

Neural Likelihood Surfaces for Spatial Processes with Computationally Intensive or Intractable Likelihoods

Julia Walchessen

Department of Statistics and Data Science, Carnegie Mellon University
and

Amanda Lenzi

School of Mathematics, University of Edinburgh
and

Mikael Kuusela

Department of Statistics and Data Science, Carnegie Mellon University

May 9, 2023

Abstract

In spatial statistics, fast and accurate parameter estimation coupled with a reliable means of uncertainty quantification can be a challenging task when fitting a spatial process to real-world data because the likelihood function might be slow to evaluate or intractable. In this work, we propose using convolutional neural networks (CNNs) to learn the likelihood function of a spatial process. Through a specifically designed classification task, our neural network implicitly learns the likelihood function, even in situations where the exact likelihood is not explicitly available. Once trained on the classification task, our neural network is calibrated using Platt scaling which improves the accuracy of the neural likelihood surfaces. To demonstrate our approach, we compare maximum likelihood estimates and approximate confidence regions constructed from the neural likelihood surface with the equivalent for exact or approximate likelihood for two different spatial processes—a Gaussian Process, which has a computationally intensive likelihood function for large datasets, and a Brown–Resnick Process, which has an intractable likelihood function. We also compare the neural likelihood surfaces to the exact and approximate likelihood surfaces for the Gaussian Process and Brown–Resnick Process, respectively. We conclude that our method provides fast and accurate parameter estimation with a reliable method of uncertainty quantification in situations where standard methods are either undesirably slow or inaccurate.

Keywords: likelihood-free inference, simulation-based inference, deep neural networks, parameter estimation, uncertainty quantification, spatial extremes

1 Introduction

In spatial statistics, parametric spatial models used to describe real-world phenomena typically have intractable or computationally intensive likelihood functions. This is generally due to the large number of spatial locations the spatial model must cover. Classical methods of statistical inference rely strongly on the likelihood function to provide parameter estimation, hypothesis testing, and uncertainty quantification (Casella and Berger, 2001). Due to this reliance, past research in the field of spatial statistics has focused on providing approximations for the likelihood that sidestep the need to evaluate the full likelihood (Sun et al., 2012). Examples include composite likelihood, low-rank approximations, and Vecchia approximation in which only a subset of spatial locations is utilized (Padoan et al., 2010; Sun et al., 2012). Yet, these approximations suffer in terms of the accuracy of estimation and uncertainty quantification compared to the statistical properties of exact likelihood (Sun et al., 2012).

Thanks to the advent of modern machine learning and the ability to quickly simulate from many spatial processes, recent research has focused on neural prediction—efficient parameter estimation using neural networks—for these processes. To address the computational inefficiency of Gaussian process parameter estimation, Gerber and Nychka (2021) trained a neural network to predict the parameters of the covariance function and achieved similar accuracy yet significant computational efficiency when compared to directly computing the maximum likelihood estimator (MLE) using the exact likelihood. Lenzi et al. (2023) demonstrated that parameter estimation using neural networks can be extended to spatial processes beyond Gaussian processes by training a neural network to predict the parameters of several max-stable processes, popular processes for modeling spatial extreme events (Davison et al., 2012). These two methods of neural prediction focused primarily on predicting the parameters of a given spatial process based on a single realization. In Gerber and Nychka (2021), the multiple realizations case is addressed by either averaging all the n neural estimators of each of the n single realizations or training a new neural network which accepts only n spatial field realizations as input and outputs a point prediction. In Sainsbury-Dale et al. (2023), these two methods are bypassed with a permutation-invariant

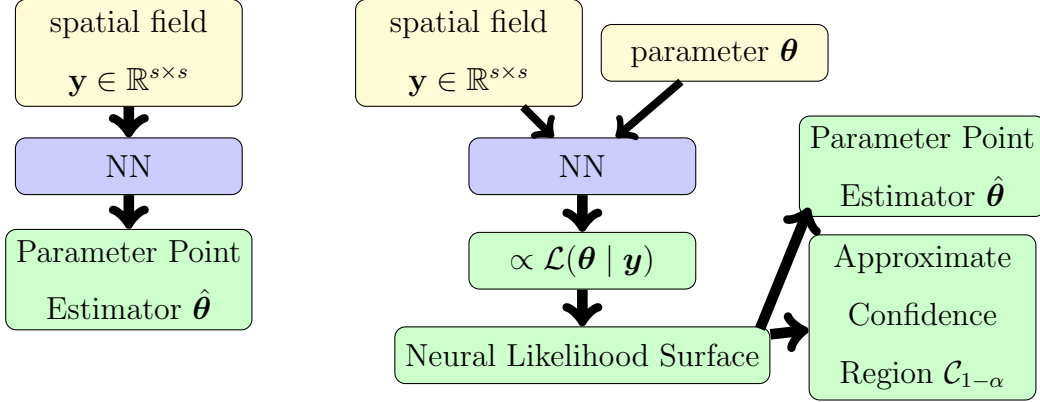


Figure 1: The basic structure for traditional neural prediction (left) and learning the likelihood via our proposed method (right) where NN refers to neural network.

neural network to learn Bayesian estimators based on multiple i.i.d realizations from a given spatial process.

While all these methods focused on parameter point prediction using neural networks, Lenzi et al. (2023); Sainsbury-Dale et al. (2023) also proposed a method for uncertainty quantification with bootstrapping, a computationally intensive approach with unclear theoretical and practical properties in this context. Unfortunately, neural prediction does not easily lend itself to more traditional, better-understood methods of quantifying uncertainty. Another limitation of neural prediction is the reliance on a prior over the parameter space. In this context, the prior corresponds to the distribution that was used to simulate the parameters for training the neural network. Depending on the prior selected, the neural network may produce biased estimates and unreliable bootstrapped uncertainty quantification. The prior dependence of neural prediction can be established with a simple argument: Since the neural estimator $\hat{\theta}$ is the minimizer of the mean squared error, it can be understood as a regularized finite-sample estimator of the conditional expectation $\mathbb{E}(\theta | \mathbf{y})$. This conditional expectation is taken with respect to the conditional distribution $p(\theta | \mathbf{y}) \propto p(\mathbf{y} | \theta)p(\theta)$ which inescapably depends on the prior $p(\theta)$. Finding a way to learn the actual likelihood function instead of point predictions has the potential to address both of these limitations of neural prediction.

In this paper, we propose a method to learn the likelihood functions of spatial processes

for which fast simulation is possible using a specifically constructed binary classification task and apply this method to processes with intractable or computationally intensive likelihoods. For the selected spatial process, fast simulation is necessary because we use simulations to form two classes consisting of pairs of a parameter $\boldsymbol{\theta}$ and a spatial field realization \mathbf{y} . The parameter $\boldsymbol{\theta}$ and spatial field \mathbf{y} are dependent in the first class and independent in the second class. Yet, the marginal distributions for both classes are the same due to a permutation trick where we form the data for the second class from the first class by permuting the parameters assigned to the realizations in the first class. We train a classifier to discriminate between these two classes and show that the resulting classifier is related to the likelihood of the spatial process via a closed-form transformation. Using the classifier and this transformation, we can produce learned likelihood surfaces, parameter estimates, and confidence regions.

Since convolutional neural networks (CNN) have excellent empirical performance in tasks involving image data, we use a CNN as our classifier. For neural prediction, Lenzi et al. (2023); Gerber and Nychka (2021); Sainsbury-Dale et al. (2023) used CNNs as well. However, a key distinction between neural prediction and our method is the inputs for the CNNs—a single input, a spatial field \mathbf{y} , for neural prediction and two inputs, a spatial field \mathbf{y} and parameter $\boldsymbol{\theta}$, for our method. See Figure 1 to better understand the basic differences between neural prediction and our method.

Learning the likelihood accurately requires our CNN to be well calibrated so we apply post-hoc calibration to it using Platt scaling (Guo et al., 2017). Calibration significantly improves the predicted probabilities from the CNN and hence the learned likelihood. As such, calibration is an integral part of our method of learning the likelihood. We refer to the likelihood function that we compute based on the final trained and calibrated CNN as neural likelihood.

As a proof of concept, we first apply our method to Gaussian processes, the most popular stochastic process for modeling spatial data, and show that the neural likelihood is comparable to the exact likelihood in terms of parameter estimation and uncertainty quantification with a significant speedup in computation. Since this method of learning

the likelihood is primarily intended for spatial processes with intractable likelihoods, we next test our method on a Brown–Resnick process, a model for spatial extremes with an intractable likelihood even for a moderate number of spatial locations, and demonstrate that the neural likelihood is comparable or better than standard methods for approximating this likelihood in terms of parameter estimation, uncertainty quantification, and computational efficiency.

A major benefit of neural likelihood over prediction-based approaches is that it is independent of the prior over the parameter space used to generate training data for the neural network. As mentioned above, prediction-based estimators have the potential to suffer from bias depending on the selected prior over the parameter space. For our proposed method, the prior over the parameter space only affects how quickly or to what detail the neural network implicitly learns the likelihood not whether bias is introduced to the neural likelihood.

Our proposed method produces parameter estimates grounded in classical statistical inference. To produce parameter estimates, we produce the neural likelihood surface on a fine grid over the parameter space and find the maximum likelihood estimator (MLE) over this grid. As will be explained later, the neural likelihood is particularly well suited for grid evaluations like this in terms of computational efficiency. Since we use grid search rather than gradient descent as most methods do, our method is likely to find the global maximizer even in the case of a non-concave likelihood surface whereas other methods might not.

By learning the likelihood, we can provide a means of uncertainty quantification using approximate confidence regions derived from the shape of the likelihood surface. These confidence regions are constructed using likelihood ratios as shown later in this paper. While these confidence regions only provide approximate finite-sample guarantees, empirically we find well-calibrated coverage for these regions for both Gaussian and Brown–Resnick process parameters.

Finally, the last two benefits of our method are computational efficiency and the ability to easily handle multiple realizations. First, compared to traditional methods of computing

the exact or approximate likelihood, our method is significantly faster by potentially several orders of magnitude depending on the process in question and the number of observed spatial locations. In the field of spatial statistics, a long line of research has focused on methods to speed up the evaluation of the likelihood for tractable spatial processes, especially the Gaussian process. Since evaluating the likelihood of a Gaussian process involves a computationally expensive inversion of the covariance matrix, most methods to speed up evaluation focus on approximating the covariance matrix with a sparse or low-rank matrix which is faster to invert. Since neural networks consist of simple non-linear and linear functions composed together, evaluating the neural likelihood can be more efficient by orders of magnitude than evaluating the exact likelihood of a Gaussian process and potentially also other tractable spatial processes depending on the number of observed spatial locations. In our case study, producing a neural likelihood surface is faster than producing an exact likelihood surface by a factor of approximately 30 for a realization of a Gaussian process with $25 \times 25 = 625$ observed spatial locations. As the size of the spatial data grows, we expect the computational efficiency to further increase significantly. Lastly, since the likelihood of multiple independent realizations is the product of the single-realization likelihoods, we can handle an arbitrary number of realizations without retraining the neural network unlike the estimators proposed in Lenzi et al. (2023); Gerber and Nychka (2021); Sainsbury-Dale et al. (2023).

Our method of learning the likelihood is not constrained to spatial processes in that the main ideas are applicable to any parametric statistical model for which fast simulation is possible. Techniques for learning the likelihood of simulator-based models have been researched extensively in certain areas of the physical sciences, especially in high energy physics (Brehmer et al., 2018; Cranmer et al., 2020). The development of methods to navigate statistical inference for stochastic processes or mechanistic models with intractable likelihoods is referred to as likelihood-free inference or simulation-based inference (Cranmer et al., 2020; Dalmaso et al., 2023). In the next section, we describe in further detail the evolution of simulation-based inference and how our proposed method is derived from this evolution.

The structure of the rest of this paper is as follows. Section 2 details how simulation-based inference has evolved with the aid of modern machine learning and how the field of spatial statistics has previously addressed inference for spatial processes with intractable or computationally intensive likelihoods. Section 3 describes our method of learning the likelihood including how the classifier relates to the likelihood, how the training data for the classification task is generated using simulation, why we use a neural network as the classifier, and how to produce neural likelihood surfaces, parameter estimates, and approximate confidence regions from the classifier. In Section 4, we study our method on two spatial processes—Gaussian and Brown–Resnick processes—and compare the resulting neural likelihood surfaces, parameter estimates, and confidence regions to those resulting from conventional methods. Finally in Section 5, we discuss the limitations of our method and possible future extensions as well as the broader implications of this work.

2 Background and Related Work

Thanks to advances in computing power and data storage, there is great interest in the collection, storage, and analysis of increasingly large spatial datasets. As a result, recent developments in the field of spatial statistics have focused on adapting classical statistical methods such as likelihood inference for large spatial data (Sun et al., 2012). In conjunction, the field of simulation-based inference has seen tremendous development in methods for learning surrogate likelihoods, likelihood ratios, and posteriors for high-dimensional data with the help of machine learning (Cranmer et al., 2020). In this section, we briefly describe relevant developments in both spatial statistics and simulation-based inference which provide the backdrop for our proposed method of learning the likelihood.

2.1 Simulation-Based Inference

In simulation-based inference, there are two classical approaches. The first is Approximate Bayesian Computation (ABC) in which simulated and observed data are compared using a distance metric and typically a summary statistic to obtain samples from an approximate

posterior (Sisson et al., 2018). The second approach is density estimation (approximate frequentist computation) in which the distribution of the simulated data or summary statistics of the simulated data is approximated using traditional methods of density estimation (Cranmer et al., 2020). Both methods suffer from the curse of dimensionality: in some cases, the number of simulations necessary for sufficient approximation grows exponentially with the dimension. The efficiency of both classical approaches to simulation-based inference can be improved by utilizing machine learning which can more easily handle larger-dimensional data (Cranmer et al., 2020).

Beyond improving traditional approaches of simulation-based inference, machine learning has ushered in a new approach in which a surrogate for the likelihood or likelihood ratio is learned using training data generated from the simulator (Dalmasso et al., 2023; Brehmer and Cranmer, 2022; Brehmer et al., 2018). As far as we are aware, there are three main approaches to learning the surrogate (Brehmer and Cranmer, 2022). The first approach is neural density estimators which are flexible probabilistic models with tractable likelihoods that can be combined in such a way as to provide a sufficient surrogate for the likelihood. This approach differs from our proposed method by approximating also the normalizing constant $p(\mathbf{y})$ where \mathbf{y} is the observed data. Since parameter estimation and uncertainty quantification using the likelihood do not hinge on learning the normalizing constant $p(\mathbf{y})$, our proposed method is potentially much faster and less tricky to train than neural density estimation.

The second approach is learning the likelihood ratio via classification and a transformation utilizing the likelihood ratio trick (Brehmer and Cranmer, 2022). This approach is referred to as CARL and is most similar to our proposed method. The first similarity between CARL and our proposed method is the transformation of the classifier output to produce the likelihood ratio. The second similarity between these methods lies in the classification task. In CARL, learning the likelihood ratio is dependent on the classification task of differentiating simulated data from the distribution of interest $\mathbf{y} \sim p(\mathbf{y} \mid \boldsymbol{\theta})$ and simulated data from a reference distribution $\mathbf{y} \sim p_{\text{ref}}(\mathbf{y})$ with fixed parameters (Brehmer and Cranmer, 2022). In our proposed method, the classification task is to differentiate between

simulated data and parameters which generated the simulated data and simulated data and parameters which did not generate the simulated data. Hence, the learning task and the construction of the training data are slightly different from CARL, but the high-level idea originates from that approach.

Finally, the third approach involves incorporating knowledge about the inner workings of the simulator, such as latent variables, into learning the surrogate (Brehmer et al., 2018; Brehmer and Cranmer, 2022). This third approach is most ideal for physical models in which there are typically latent variables and some knowledge of the simulator. This approach could also be helpful for simulation-based inference for hierarchical statistical models. However, in the absence of a hierarchical model and in the interest of full generality, we will focus in this paper on simulation-based inference that does not attempt to make explicit use of latent variables.

To the best of our knowledge, simulation-based inference for learning the likelihood has not been previously applied to spatial statistics or purely statistical modeling in general. As such, we believe that our approach is novel in the field of spatial statistics, yet it is well-grounded in recent developments within the field of simulation-based inference, especially as used in high-energy physics. Furthermore, certain details of our approach for learning the likelihood, such as the permutation method for forming the two training classes, appear to be unique and may provide advantages over existing methods.

2.2 Spatial Statistics

In spatial statistics, work on likelihood-based inference methods focuses on either expediting the process of evaluating the exact likelihood for spatial processes with tractable likelihoods or providing an approximation of the likelihood for spatial processes with intractable likelihoods.

Often, when evaluating exact likelihoods of spatial processes over a large number of spatial locations, the covariance matrix must be inverted, as is the case of Gaussian processes, for example (Sun et al., 2012). The time complexity and memory required for matrix inversion are $\mathcal{O}(n^3)$ and $\mathcal{O}(n^2)$, respectively, where n is the number of spatial locations (Sun

et al., 2012, p. 56). To reduce the time complexity of matrix inversion, there are two main approaches—representing the original covariance matrix as a low-rank matrix or as a sparse matrix (Heaton et al., 2017). Low-rank and sparse matrices are much faster to invert than the original covariance matrix. Yet, these representations of the original covariance matrix contain less information about the spatial process which can lead to reduced accuracy in parameter estimation and uncertainty quantification as well as a lack of statistical guarantees (Sun et al., 2012).

For Gaussian random fields (GRFs), Lindgren et al. (2011) modeled the spatial field as a solution of an Stochastic Partial Differential Equation (SPDE) and showed that inference is of the order $\mathcal{O}(n^{3/2})$ compared to the $\mathcal{O}(n^3)$ complexity for estimating covariance functions. These computational benefits are due to estimating precision matrices (inverse covariance matrices) rather than covariance matrices. Whereas covariance matrices of GRFs are primarily dense, several standard models have sparse precision matrices, with a Markovian structure where only close neighbours are non-zero due to the conditional independence between the random variables in the multivariate Gaussian distribution. However, there are several important classes of spatial processes, such as non-Gaussian models for spatial extremes, that cannot be handled using the SPDE approach.

Another popular method for efficiently evaluating the likelihood of a Gaussian process is Vecchia approximation (Sun et al., 2012; Katzfuss and Guinness, 2021). The motivation for the Vecchia approximation comes from the observation that the joint density of a spatial process observed at multiple spatial locations can be written as the product of conditional densities according to some ordering of the spatial locations. In Vecchia approximation, computing this product of conditional densities is made more efficient by reducing the number of conditioning locations used to compute the conditional densities in the product. Due to the decision to reduce the number of conditioned spatial locations, Vecchia approximation loses information about the full likelihood and requires design choices as to how to order the spatial locations and which spatial locations to not include in the conditioning.

While we cover composite likelihood for Brown–Resnick processes in greater depth in Section 4, we provide a general description of composite likelihood here. Composite likeli-

hood is applicable to many max-stable processes for which the likelihood is tractable only up to a certain number of spatial locations (Castruccio et al., 2016). For these spatial processes, the full likelihood involves a summation indexed by the number of partitions for n spatial locations which grows more than exponentially with respect to n . Due to this more than exponential growth, the full likelihood is intractable for large and even moderate n . Yet, if we approximate the likelihood with a product of m -variate densities for $m \ll n$, such as the bivariate density, we reduce the number of terms to consider. However, even this reduction in terms can be too intensive to compute, and consequentially, only a subset of spatial locations are typically used in the m -variate densities (Padoan et al., 2010). As with Vecchia approximation, composite likelihood contains less information about the full likelihood and requires a design choice in terms of which subsets of spatial locations to include. A poor design choice may lead to a significant deterioration in the quality of the inferences, as shown in Section 4.3.2 for the Brown–Resnick process.

In all the techniques outlined in this (non-exhaustive) overview of methods for evaluating or approximating likelihoods for large spatial data, there are common themes in terms of loss of information and the necessity of nontrivial design choices to achieve an approximation of the full likelihood. Our proposed method learns the full likelihood and only requires design choices in terms of the neural network structure and training hyperparameters, choices that are easy to optimize using a validation dataset. Finally, many of these previous techniques are specific to certain types of spatial processes, whereas our method of learning the likelihood is generalizable to any spatial process on a grid (in fact, any statistical model with regular outputs) for which fast simulation is possible.

3 Methodology

This section describes our framework for learning the likelihood function from a specifically-designed classification task using simulated data from a given spatial process. Specifically, our task is to infer the parameter $\boldsymbol{\theta}$ from a realization \mathbf{y} of a spatial process evaluated on

a finite set of spatial locations:

$$\begin{aligned} f &\sim \text{SpatialProcess}(\boldsymbol{\theta}), \\ \mathbf{y} &:= f(\mathcal{S}), \end{aligned} \tag{1}$$

where \mathcal{S} is a set of spatial locations on which we observe a realization f from a spatial process depending on an unknown parameter $\boldsymbol{\theta}$. A key assumption throughout this work is that for any $\boldsymbol{\theta}$, it is easy to simulate realizations \mathbf{y} from $\text{SpatialProcess}(\boldsymbol{\theta})$ according to Equation (1).

3.1 Connection between Simulated Data, Classification Task, and Likelihood

Our methodology hinges on four key observations. First, simulation from many spatial processes with intractable likelihoods is simple and fast. Fast simulation enables us to apply likelihood-free inference techniques to these intractable spatial processes in order to learn the likelihood (Cranmer et al., 2020). Second, the realizations from spatial processes with different parameters may be distinguishable by the well-trained eye, and as such, one would expect an image classification model such as a convolutional neural network (CNN) to be able to distinguish between realizations generated by different parameters. Third, modern classification algorithms are not necessarily affected by the curse of dimensionality to the same extent as other methods of directly learning the likelihood might be. Finally, we can draw the connection below between a specifically-designed classification task and the likelihood function of a given spatial process using a permutation-based approach described in Section 3.2. While connections between classifiers and likelihoods have been made before in simulation-based inference as mentioned in Section 2, this particular method of connecting the classifier to the likelihood using a permutation-based approach appears to be new and forms the foundation of our method.

Consider the space $D \times \Theta$, where D is the space of realizations for some spatial process evaluated on spatial locations \mathcal{S} governed by parameters from the parameter space Θ which we assume to be bounded. We will relate the likelihood function $\mathcal{L}(\boldsymbol{\theta} \mid \mathbf{y}) = p(\mathbf{y} \mid \boldsymbol{\theta})$ for parameter $\boldsymbol{\theta} \in \Theta$ and realization $\mathbf{y} \in D$ to the output of a probabilistic binary classifier

$h : D \times \Theta \rightarrow [0, 1], (\mathbf{y}, \boldsymbol{\theta}) \mapsto h(\mathbf{y}, \boldsymbol{\theta})$. The first class ($C = 1$) for the binary classifier is the class in which pairs of realizations and parameters are dependent. Specifically, the given realization \mathbf{y} is generated from the spatial process with the given parameter $\boldsymbol{\theta}$. The second class ($C = 2$) is the class in which the pairs of realizations and parameters are independent yet have the same marginal distributions as in the first class. The conditional probabilities for the two classes have the following form:

$$P((\mathbf{y}, \boldsymbol{\theta}) \mid C = 1) = p(\mathbf{y}, \boldsymbol{\theta}) \quad \text{and} \quad P((\mathbf{y}, \boldsymbol{\theta}) \mid C = 2) = p(\mathbf{y})p(\boldsymbol{\theta}), \quad (2)$$

where $p(\mathbf{y})$ and $p(\boldsymbol{\theta})$ are the marginal distributions implied by $p(\mathbf{y}, \boldsymbol{\theta})$,

$$p(\mathbf{y}) = \int p(\mathbf{y}, \boldsymbol{\theta}) d\boldsymbol{\theta} \quad \text{and} \quad p(\boldsymbol{\theta}) = \int p(\mathbf{y}, \boldsymbol{\theta}) d\mathbf{y}. \quad (3)$$

We can now draw the connection between our constructed classifier $h(\mathbf{y}, \boldsymbol{\theta})$ and the likelihood function $\mathcal{L}(\boldsymbol{\theta} \mid \mathbf{y})$:

$$\begin{aligned} h(\mathbf{y}, \boldsymbol{\theta}) &= P(C = 1 \mid (\mathbf{y}, \boldsymbol{\theta})) = \frac{P((\mathbf{y}, \boldsymbol{\theta}) \mid C = 1)P(C = 1)}{P((\mathbf{y}, \boldsymbol{\theta}) \mid C = 1)P(C = 1) + P((\mathbf{y}, \boldsymbol{\theta}) \mid C = 2)P(C = 2)} \\ &= \frac{\frac{P((\mathbf{y}, \boldsymbol{\theta}) \mid C=1)}{P((\mathbf{y}, \boldsymbol{\theta}) \mid C=2)}}{\frac{P((\mathbf{y}, \boldsymbol{\theta}) \mid C=1)}{P((\mathbf{y}, \boldsymbol{\theta}) \mid C=2)} + 1} = \frac{\frac{p(\mathbf{y}, \boldsymbol{\theta})}{p(\mathbf{y})p(\boldsymbol{\theta})}}{\frac{p(\mathbf{y}, \boldsymbol{\theta})}{p(\mathbf{y})p(\boldsymbol{\theta})} + 1} = \frac{p(\mathbf{y})^{-1}p(\mathbf{y} \mid \boldsymbol{\theta})}{p(\mathbf{y})^{-1}p(\mathbf{y} \mid \boldsymbol{\theta}) + 1} = \frac{p(\mathbf{y})^{-1}\mathcal{L}(\boldsymbol{\theta} \mid \mathbf{y})}{p(\mathbf{y})^{-1}\mathcal{L}(\boldsymbol{\theta} \mid \mathbf{y}) + 1}. \end{aligned} \quad (4)$$

On the first line of (4), we apply Bayes' Rule in order to describe the classifier output $h(\mathbf{y}, \boldsymbol{\theta})$ in terms of the conditional probabilities for the two classes. In the second line, we use (2) and assume the two classes are balanced, i.e., $P(C = 1) = P(C = 2) = 1/2$, for ease of exposition.

To more clearly connect the classifier and the likelihood function, we define a function $\psi : D \times \Theta \rightarrow \mathbb{R}$ in the following way:

$$\psi(\mathbf{y}, \boldsymbol{\theta}) = p(\mathbf{y})^{-1}\mathcal{L}(\boldsymbol{\theta} \mid \mathbf{y}). \quad (5)$$

Substituting the function ψ into (4), we obtain

$$h(\mathbf{y}, \boldsymbol{\theta}) = \frac{\psi(\mathbf{y}, \boldsymbol{\theta})}{\psi(\mathbf{y}, \boldsymbol{\theta}) + 1}. \quad (6)$$

We can solve (6) for ψ which is proportional to the likelihood function $\mathcal{L}(\boldsymbol{\theta} \mid \mathbf{y})$ for a fixed realization \mathbf{y} :

$$\mathcal{L}(\boldsymbol{\theta} \mid \mathbf{y}) \propto \psi(\mathbf{y}, \boldsymbol{\theta}) = \frac{h(\mathbf{y}, \boldsymbol{\theta})}{1 - h(\mathbf{y}, \boldsymbol{\theta})}. \quad (7)$$

This shows that the likelihood function is proportional to a simple transformation of the classifier output h .

If desired, we can also use the same classifier h to evaluate the likelihood (up to a multiplicative constant) for an arbitrary number of i.i.d. realizations $\mathbf{y}_1, \dots, \mathbf{y}_n$ from a common spatial process in the following manner:

$$\mathcal{L}(\boldsymbol{\theta} \mid \mathbf{y}_1, \dots, \mathbf{y}_n) = \prod_{i=1}^n \mathcal{L}(\boldsymbol{\theta} \mid \mathbf{y}_i) \propto \prod_{i=1}^n \psi(\mathbf{y}_i, \boldsymbol{\theta}) = \prod_{i=1}^n \frac{h(\mathbf{y}_i, \boldsymbol{\theta})}{1 - h(\mathbf{y}_i, \boldsymbol{\theta})}. \quad (8)$$

Notice that there is no need to change the classifier h if n changes.

In the following section, we explain how to construct the two classes for training a classifier \hat{h} which estimates the exact classifier h from finite simulated data. With the estimator \hat{h} , we can use (5) and (7) to obtain the estimated neural likelihood,

$$\mathcal{L}_{\text{NN}}(\boldsymbol{\theta} \mid \mathbf{y}) := p(\mathbf{y})\hat{\psi}(\mathbf{y}, \boldsymbol{\theta}) \propto \hat{\psi}(\mathbf{y}, \boldsymbol{\theta}) = \frac{\hat{h}(\mathbf{y}, \boldsymbol{\theta})}{1 - \hat{h}(\mathbf{y}, \boldsymbol{\theta})}. \quad (9)$$

3.2 Generating the two specifically constructed classes via simulation

In order to train the classifier $\hat{h} : D \times \Theta \rightarrow [0, 1]$ which is an estimator of the exact classifier h in (4), we need to first obtain samples from the two classes described above. To produce the first class ($C = 1$), we simulate realizations \mathbf{y} from the spatial process for different parameters $\boldsymbol{\theta} \in \Theta$ and pair the simulated realizations with the parameter which generated the realization. To produce the second class ($C = 2$), we simply permute the parameters assigned to the simulated realizations in the first class to break the dependency between the two while maintaining the marginal distributions. By permuting the parameters in the first class, we eliminate the need to simulate more data, saving computing time and storage space. In the following paragraphs, we describe in detail how the classes are constructed using simulation and permutation and provide pseudocode for the construction process in Algorithms 1 and 2.

Algorithm 1 Generating Data for First Class

```
for  $i$  in  $1 : m$  do  
     $\theta_i \sim \text{LHS}(\Theta)$   
    for  $j$  in  $1 : n$  do  
         $f_{i,j} \sim \text{SpatialProcess}(\theta_i)$   
         $y_{i,j} = f_{i,j}(\mathcal{S})$   
    end for  
end for
```

The first class is $C_1 = \{(y_{i,j}, \theta_i)\}_{i \in [m], j \in [n]}$.

First, we sample m parameters from the bounded parameter space Θ in such a way that the sampled parameters are guaranteed to uniformly cover Θ . It is key to note that Θ must be bounded in order to obtain samples from Θ which accurately represent the whole parameter space of interest. It is also important to note that the sampling method for Θ is not a prior over Θ in the Bayesian sense. Our method of learning the likelihood does not require any priors over Θ in the Bayesian sense. Yet, a poor sampling method that does not provide sufficient coverage of Θ will result in a neural likelihood surface with less information about the true likelihood in certain regions of Θ . To avoid this, we utilize Latin hypercube sampling (LHS) using the LHS R package (Carnell, 2022). In Latin hypercube sampling, Θ is partitioned into m equal sized regions, and a parameter θ_i is sampled from each of these m regions and forms the sampled parameters $\{\theta\}_{i \in [m]}$. As such, Latin hypercube sampling guarantees that the sampled parameters $\{\theta\}_{i \in [m]}$ provide uniform coverage of Θ .

Next, for each sampled parameter, we simulate n realizations from the spatial process evaluated at locations \mathcal{S} . We will specify what \mathcal{S} is in Section 3.3. The $n \cdot m$ pairs of realizations and the sampled parameters which generated the realizations will form the first class. The sampling process for the first class is summarized in Algorithm 1.

After simulating data for the first class, we can construct the independent pairs of realizations and parameters from the dependent pairs of the first class using permutations of the sampled parameters. Since there are m sampled parameters and n realizations

Algorithm 2 Constructing Second Class from First Class

Sample uniformly at random n permutations $\pi_1 \cdots \pi_n$ of indices $1 \dots m$

Initialize $C_2 = \emptyset$

for j in $1 : n$ **do**

$C_2 \leftarrow C_2 \cup \{(\mathbf{y}_{i,j}, \boldsymbol{\theta}_{\pi_j(i)}) \mid i \in [m]\}$

end for

The second class is $C_2 = \{(\mathbf{y}_{i,j}, \boldsymbol{\theta}_{\pi_j(i)}) \mid i \in [m], j \in [n]\}$.

per sampled parameter, we randomly sample n permutations of the indices 1 through m which we refer to as π_1, \dots, π_n . For the j th realizations of the spatial fields, we apply the permutation π_j to the sampled parameters and assign each of the permuted parameters to the corresponding spatial field realization to obtain pairs of the following form:

$$\{(\mathbf{y}_{i,j}, \boldsymbol{\theta}_{\pi_j(i)}) \mid i \in [m]\}. \quad (10)$$

We repeat this process for all n values of the index j . The spatial field realizations and permuted parameters are now independent of each other with unchanged marginal distributions by construction, as required. Due to this process of permuting the sampled parameters, we avoid simulating and storing new data for the second class. Pseudocode for the process of constructing the second class from the first class is shown in Algorithm 2. See Figure 2 for an illustration of the first and second classes to more fully understand the permutation process.

3.3 Classifier Architecture

Now that we have described how to learn the likelihood using specifically constructed classes, we need to select a classifier that can be flexible both in input shape and structure. As of yet, we have not specified the set of spatial locations \mathcal{S} for the evaluation of the spatial process. In this paper, we restrict the set of spatial locations \mathcal{S} to a regular grid of fixed size and discuss the potential to relax this restriction in Section 5. The classifier

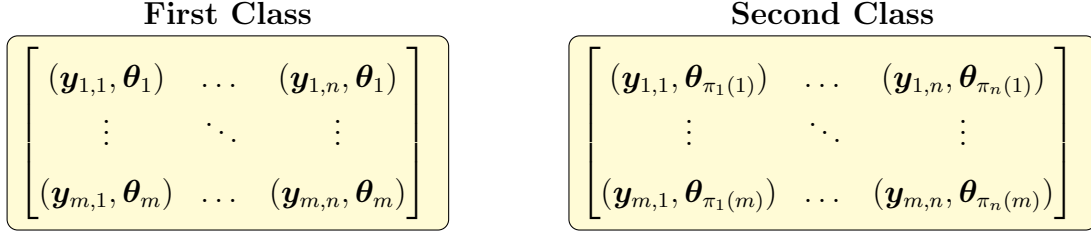


Figure 2: A visualization of the pairs of spatial field realizations \mathbf{y} and parameters $\boldsymbol{\theta}$ in the first and second classes. For both classes, the realizations $\mathbf{y}_{i,j}$ in the i th row are generated using the same parameter $\boldsymbol{\theta}_i$. In the first class, all realizations $\mathbf{y}_{i,j}$ are paired with the parameter $\boldsymbol{\theta}_i$ which generated the realization. In the second class, the realizations $\mathbf{y}_{i,j}$ in the j th column are paired with parameters permuted according to the j th permutation of the total number of parameters- m .

needs to be flexible enough in structure to accommodate many different spatial processes since our method of learning the likelihood through classification is in principle applicable to any spatial process. For instance, the classifier needs to be flexible enough to learn intractable likelihoods, which might have complicated, unusual shapes, as well as simpler, more familiar likelihoods, such as the likelihood of a Gaussian process with some simple covariance function. Since artificial neural networks are both flexible in input shape and structure and flexible in the complexity of the functions they can approximate, we use a convolutional neural network (CNN) with a specific structure to accommodate the spatial field input \mathbf{y} , a matrix of fixed size, and the parameter $\boldsymbol{\theta}$, a vector of fixed size. CNNs have previously been used by Lenzi et al. (2023); Gerber and Nychka (2021); Sainsbury-Dale et al. (2023) to predict parameters of spatial fields, and we continue this practice here, with appropriate modifications as detailed below, because CNNs are excellent at handling images, and the spatial field input \mathbf{y} is effectively an image.

The following offers a brief overview of CNNs as used here. For those interested in a more detailed description, we refer the reader to Lecun et al. (1998), the original paper introducing CNNs, and Chapter 9 of Goodfellow et al. (2016). A CNN is a type of artificial neural network which takes as input a matrix of fixed size and uses convolutions to extract spatial patterns between matrix entries pertinent to the task in question (Goodfellow et al., 2016, pp. 329–341). Specifically, filters in each convolutional layer of the CNN extract

different spatial patterns that may be of use in the learning task. Due to their ability to extract spatial patterns, CNNs are often used to process visual data such as photos in which pixels can be depicted as constituting a fixed-size matrix. As such, CNNs are well suited to dealing with the spatial field input which is effectively an image. Outputs of a CNN can vary from a scalar in the case of binary classification, as in our case here, to a multidimensional vector in the case of multi-class classification or even another matrix in the case of image-on-image regression (Goodfellow et al., 2016, pp. 352–353).

In a CNN, convolutional layers are interspersed with pooling layers in order to distill the spatial information contained in an image or other matrix-type object to the most important spatial patterns. Pooling layers reduce the size of the output of the previous layer by combining multiple neurons into a single neuron in the next layer (Goodfellow et al., 2016, pp. 335–339). An example of pooling is *max pooling* in which the maximum value of multiple neurons in the previous convolutional layer becomes the value of a neuron in the next convolutional layer. The output of the convolutional and pooling layers is a reduced-size matrix containing spatial patterns or features of interest to the learning task.

In the case of classification, this reduced matrix can be flattened to a manageable-size vector which is then processed in the second part of the network—a collection of fully connected layers with multiple hidden layers ending with an output layer. For binary classification, the output layer is either a binary classification output or a class probability, a real value between zero and one, depending on the activation function as well as the loss function. In our case, the output is $\hat{h}(\mathbf{y}, \boldsymbol{\theta}) = \hat{P}(C = 1 \mid (\mathbf{y}, \boldsymbol{\theta}))$ which we obtain by using the sigmoid activation function and binary cross-entropy loss (Goodfellow et al., 2016, p. 130).

Since the input for our classifier is both a matrix, the spatial field \mathbf{y} , and a vector, the parameter $\boldsymbol{\theta}$, we need to modify the structure of a typical CNN to accommodate this type of input. As noted above, the first part of a CNN classifier produces a flattened vector after multiple convolutional and pooling layers. For our CNN classifier, we first transform the spatial field into a flattened vector of reduced dimension via the convolutional part of the CNN classifier. Since the flattened vector and the parameter $\boldsymbol{\theta}$ are both in vector

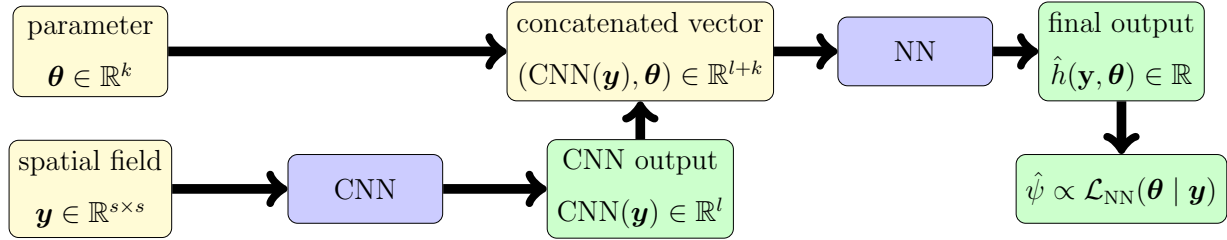


Figure 3: The basic structure of our CNN. In this illustration, CNN refers to the convolutional and pooling layers and NN refers to the fully connected layers.

form, we can concatenate the two and process the concatenated vector with the fully connected part of the CNN classifier where the last layer outputs the desired class probability. Figure 3 illustrates this CNN architecture. In Figure 3, we refer to the convolutional part as CNN and the fully connected part as NN. We implement this CNN classifier using the Keras interface (Chollet et al., 2015) for Tensorflow and train the network using the Adam optimizer (Kingma and Ba, 2015).

3.4 Calibration

Due to growth in model capacity, modern neural networks are not always well-calibrated (Guo et al., 2017). A classification model is well-calibrated when the estimated class probability for a given input is sufficiently close to the true probability of the input belonging to the given class. For binary classification, perfect calibration is defined as

$$P(C = 1 \mid \hat{h}(\mathbf{x}) = p) = p, \quad \forall p \in [0, 1], \quad (11)$$

where \mathbf{x} is the input and $\hat{h}(\mathbf{x}) = \hat{P}(C = 1 \mid \mathbf{x})$ is the estimated probability of the input belonging to class one (Guo et al., 2017). For neural networks, model capacity is determined by depth, which refers to the number of layers in a neural network, and width, which refers to how complex each layer is. Our CNN has the potential to suffer from miscalibration depending on the complexity of the convolutional layers which is determined by the number of filters per layer.

To correct this potential miscalibration, we utilize a calibration method called *Platt scaling* (Platt, 1999). In Platt scaling, the original class probabilities from a classifier are

used as features for a logistic regression model whose response variables are the true class labels. The fitted values of this regression are then the calibrated class probabilities. The training data for calibration is independent from the data used to train the CNN. Our logistic regression model has the following form:

$$\log \left(\frac{\pi(p)}{1 - \pi(p)} \right) = \beta_0 + \beta_1 \log \left(\frac{p}{1 - p} \right), \quad (12)$$

where p is the uncalibrated probability for class one and $\pi(p)$ is the corresponding calibrated probability. In (12), the domain of p is transformed from $[0, 1]$ to \mathbb{R}^+ which improves the logistic regression model. More details on calibration are given in Section 4. From here on, we use \hat{h} to denote the calibrated classifier.

3.5 Likelihood Inference with Neural Likelihood

In this section, we describe how to construct likelihood surfaces, parameter estimators, and approximate confidence regions using the neural likelihood. It is worth noting that the neural likelihood $\mathcal{L}_{\text{NN}}(\boldsymbol{\theta} \mid \mathbf{y}) = p(\mathbf{y})\hat{\psi}(\mathbf{y}, \boldsymbol{\theta})$ is only known up to a multiplicative constant because $p(\mathbf{y})$ is unknown. In what follows, we evaluate $\hat{\psi}(\mathbf{y}, \boldsymbol{\theta})$ over the parameter space Θ . This surface, which we refer to as the neural likelihood surface, is proportional to the likelihood $\mathcal{L}_{\text{NN}}(\boldsymbol{\theta} \mid \mathbf{y})$. As shown below, parameter estimators and approximate confidence regions are fortunately not affected by the unknown proportionality constant.

3.5.1 Constructing Neural Likelihood Surfaces

First, we explain how to obtain the neural likelihood surface over the parameter space Θ from the classifier \hat{h} for a fixed realization \mathbf{y} . Since the parameter space Θ is bounded, we evaluate the classifier $\hat{h}(\mathbf{y}, \cdot)$ on a regular grid

$$\Theta^L = \{(\theta_1 + \alpha_1 \cdot i_1, \dots, \theta_k + \alpha_k \cdot i_k)^T \mid i_j \in [s_j], j \in [k]\} \quad (13)$$

where $\alpha_1, \dots, \alpha_k > 0$ are the fixed lengths between points for the respective dimensions, $s_j \in \mathbb{N}$ are the number of points in each dimension, and θ_j and $\theta_j + \alpha_j \cdot s_j$ are the endpoints of Θ for the respective dimension. Then, we transform the classifier outputs $\hat{h}(\mathbf{y}, \boldsymbol{\theta})$ for

$\boldsymbol{\theta} \in \Theta^L$ via the transformation given in (9). This produces a regular grid of values which are proportional to the neural likelihood function $\mathcal{L}_{\text{NN}}(\cdot \mid \mathbf{y})$ evaluated on the same regular grid Θ^L for the fixed realization $\mathbf{y} \in D$.

Due to modern software packages such as the Keras interface to Tensorflow, we can quickly construct the neural likelihood surface using our CNN in the following manner (Chollet et al., 2015). For a given realization $\mathbf{y} \in D$, we evaluate the CNN with the vectorized input of the realization \mathbf{y} and parameters in the regular grid:

$$\{(\mathbf{y}, \boldsymbol{\theta}_l) \mid \boldsymbol{\theta}_l \in \Theta^L\} \quad (14)$$

to obtain the neural likelihood surface. The CNN can handle this vectorized input at once, and thus, we can efficiently evaluate the neural likelihood surface. Moreover, once trained and calibrated, the CNN is amortized and thus, we can efficiently evaluate the neural likelihood surface for multiple realizations \mathbf{y} .

To demonstrate our method, we compare our neural likelihood surface to the exact likelihood surface if available or the approximate likelihood if the the likelihood is intractable. We construct the exact or approximate likelihood surfaces using the same process including the same regular grid for neural likelihood surfaces.

Finally, the surfaces we construct are truly the log neural and log exact and log approximate likelihood surfaces. As shown in Section 3.1, the transformed classifier output $\hat{\psi}$ is equivalent to the likelihood up to a multiplicative constant. By applying a log transformation to the transformed classifier output in (9), the multiplicative constant becomes an additive constant. Consequentially, the ranges of the log neural and log exact likelihood surfaces should have the same range of values yet shifted by some unknown constant. By constructing log neural and log exact or log approximate likelihood surfaces, we facilitate comparisons between the surfaces and the construction of approximate confidence regions.

3.5.2 Constructing Parameter Estimators from neural likelihood Surfaces

Parameter estimation for the neural and exact or approximate likelihoods is a discrete version of maximum likelihood estimation (MLE) in which we select the parameter on the

grid Θ^L which maximizes the given surface.

$$\hat{\theta}_{\text{NN}} = \arg \max_{\theta \in \Theta^L} \mathcal{L}_{\text{NN}}(\theta \mid \mathbf{y}) = \arg \max_{\theta \in \Theta^L} p(\mathbf{y}) \hat{\psi}(\mathbf{y}, \theta) = \arg \max_{\theta \in \Theta^L} \hat{\psi}(\mathbf{y}, \theta) \quad (15)$$

In the rest of the paper, we refer to the parameter estimator in (15) as the neural parameter estimator $\hat{\theta}_{\text{NN}}$. Following the same process of determining the parameter which maximizes the surface over Θ^L , we produce parameter estimators for the exact and approximate likelihoods and refer to these parameter estimators as exact likelihood estimators $\hat{\theta}$ and approximate likelihood estimators $\hat{\theta}_{\text{approx}}$ respectively.

$$\hat{\theta}_{\text{approx}} = \arg \max_{\theta \in \Theta^L} \mathcal{L}_{\text{approx}}(\theta \mid \mathbf{y}) \text{ and } \hat{\theta} = \arg \max_{\theta \in \Theta^L} \mathcal{L}(\theta, \mathbf{y}) \quad (16)$$

There are two major reasons why we use a grid-based approach rather than a gradient-based approach for parameter estimation via maximum likelihood. First, due to the way we construct the neural likelihood, the exact gradient is unavailable, and an approximation of the neural likelihood gradient would be more difficult to compute than simply finding the parameter on a finite grid which maximizes the surface. Since the grid-based maximization approach is preferable for the neural likelihood, we use the same grid-based maximization approach for the exact and approximate likelihoods in order to produce a fair comparison between parameter estimators. Second, a gradient-based maximization approach may suffer from a local maxima problem whereas a grid-based maximization approach does not. If the exact likelihood were non-convex, a gradient-based approach might find a local maximum rather than a global maximum and hence potentially select a parameter far from the global maximizer. Yet, the grid-based approach would select a parameter which is reasonably close to the global maximizer over Θ depending on the resolution of the grid. Hence, the grid-based approach enables *global maximization* of the likelihood within Θ .

3.5.3 Constructing Approximate Confidence Regions from Neural Likelihood Surfaces

Next, we explain how to construct approximate confidence regions from the neural, exact, and approximate likelihood surfaces using inversion of the likelihood ratio test (Casella and Berger, 2001). Constructing confidence regions using the Fisher information may

seem to be a good approach at first glance. Yet, confidence regions constructed using the Fisher information are elliptical in shape which may not be accurate, and the Fisher information requires information about the second derivative of the likelihood which the neural likelihood does not contain (Keener, 2010). Instead, we construct approximate confidence regions using the likelihood ratio test because these confidence regions tend to have better coverage accuracy than those constructed using inversion of other asymptotic methods (Vaart, 1998).

The likelihood ratio for the exact likelihood is

$$\lambda(\boldsymbol{\theta}) = \frac{\mathcal{L}(\boldsymbol{\theta} \mid \mathbf{y})}{\mathcal{L}(\hat{\boldsymbol{\theta}} \mid \mathbf{y})}.$$

For parameters $\boldsymbol{\theta}$ with likelihoods close to the maximum likelihood, the likelihood ratio will be large and vice versa (Shao, 2003, p. 429). We reject the null hypothesis that the true parameter is θ_0 if the likelihood ratio test statistic is greater than some critical value C_α :

$$\text{reject } H_0 \text{ if } -2 \log(\lambda(\boldsymbol{\theta}_0)) = -2 \log \left(\frac{\mathcal{L}(\boldsymbol{\theta}_0 \mid \mathbf{y})}{\mathcal{L}(\hat{\boldsymbol{\theta}} \mid \mathbf{y})} \right) > C_\alpha \quad (17)$$

with $C_{1-\alpha}$ chosen so that the test has significance level α for large enough sample sizes. According to Wilk's Theorem, the asymptotic distribution of the likelihood ratio test statistic $-2 \log(\lambda(\boldsymbol{\theta}))$ is Chi-squared with degrees of freedom equal to the dimension of the parameter space Θ under the null hypothesis (Shao, 2003, p. 432). Wilk's Theorem has some conditions; the two most important conditions for our situation are the following: the true parameter which generated the data is in the interior of Θ and the likelihood is differentiable with respect to $\boldsymbol{\theta}$ (Shao, 2003, p. 287). This restriction of the true parameter to the interior of Θ will be discussed in Section 5.

We can construct a $1 - \alpha$ confidence set $C_{1-\alpha}(\Theta)$ by inverting the likelihood ratio test (Casella and Berger, 2001). The $1 - \alpha$ confidence set $C_{1-\alpha}(\Theta)$ is all parameters in Θ for which the null hypothesis in (17) is satisfied:

$$\begin{aligned} C_{1-\alpha}(\Theta) &= \{\boldsymbol{\theta} \in \Theta \mid -2 \log(\lambda(\boldsymbol{\theta})) \leq C_\alpha\} \\ &= \{\boldsymbol{\theta} \in \Theta \mid -2 \left(\log(\mathcal{L}(\boldsymbol{\theta} \mid \mathbf{y})) - \log(\mathcal{L}(\hat{\boldsymbol{\theta}} \mid \mathbf{y})) \right) \leq C_\alpha\} \\ &= \{\boldsymbol{\theta} \in \Theta \mid 2 \left(\log(\mathcal{L}(\hat{\boldsymbol{\theta}} \mid \mathbf{y})) - \log(\mathcal{L}(\boldsymbol{\theta} \mid \mathbf{y})) \right) \leq C_\alpha\}. \end{aligned} \quad (18)$$

To accommodate the evaluation of the likelihood on a regular grid, we restrict (18) to parameters on the grid $\Theta^L \subset \Theta$:

$$\mathcal{C}_{1-\alpha}(\Theta^L) = \{\boldsymbol{\theta} \in \Theta^L \mid 2\left(\log(\mathcal{L}(\hat{\boldsymbol{\theta}} \mid \mathbf{y})) - \log(\mathcal{L}(\boldsymbol{\theta} \mid \mathbf{y}))\right) \leq C_\alpha\}. \quad (19)$$

For the approximate likelihood, we simply replace $\mathcal{L}(\boldsymbol{\theta} \mid \mathbf{y})$ with $\mathcal{L}_{\text{approx}}(\boldsymbol{\theta} \mid \mathbf{y})$ in (19) to obtain $\mathcal{C}_{\text{approx},1-\alpha}(\Theta^L)$. Finally, we can replace $\mathcal{L}(\boldsymbol{\theta} \mid \mathbf{y})$ with $\hat{\psi}$ to obtain $\mathcal{C}_{\text{NN},1-\alpha}(\Theta^L)$,

$$\begin{aligned} \mathcal{C}_{\text{NN},1-\alpha}(\Theta^L) &= \{\boldsymbol{\theta} \in \Theta^L \mid 2\left(\log(\mathcal{L}_{\text{NN}}(\hat{\boldsymbol{\theta}} \mid \mathbf{y})) - \log(\mathcal{L}_{\text{NN}}(\boldsymbol{\theta} \mid \mathbf{y}))\right) \leq C_\alpha\} \\ &= \{\boldsymbol{\theta} \in \Theta^L \mid 2\left(\log(p(\mathbf{y})\hat{\psi}(\mathbf{y}, \hat{\boldsymbol{\theta}})) - \log(p(\mathbf{y})\hat{\psi}(\mathbf{y}, \boldsymbol{\theta}))\right) \leq C_\alpha\} \\ &= \{\boldsymbol{\theta} \in \Theta^L \mid 2\left(\left(\log(p(\mathbf{y})) + \log(\hat{\psi}(\mathbf{y}, \hat{\boldsymbol{\theta}}))\right) - \left(\log(p(\mathbf{y})) + \log(\hat{\psi}(\mathbf{y}, \boldsymbol{\theta}))\right)\right) \leq C_\alpha\} \\ &= \{\boldsymbol{\theta} \in \Theta^L \mid 2\left(\log(\hat{\psi}(\mathbf{y}, \hat{\boldsymbol{\theta}})) - \log(\hat{\psi}(\mathbf{y}, \boldsymbol{\theta}))\right) \leq C_\alpha\}, \end{aligned} \quad (20)$$

because the proportional constant $p(\mathbf{y})$ cancels out in (19).

The confidence region $\mathcal{C}_{1-\alpha}(\Theta^L)$ is only guaranteed $1 - \alpha$ coverage for a sufficiently large number of samples according to Wilk's Theorem (Vaart, 1998). This implies that the greater the number of realizations $\mathbf{y}_1, \dots, \mathbf{y}_n$ used to evaluate the exact or neural likelihood, the more accurate the coverage for our constructed confidence regions. For the exact or neural likelihood of a single realization \mathbf{y}_1 , the empirical coverage of the confidence regions might not match the asymptotically guaranteed value. Yet, in practice, the empirical coverage of the confidence regions appears to be close to the asymptotically guaranteed value as demonstrated in our experiments in section 4.

There are two reasons why we construct confidence regions. First, we would like to understand how reliable the neural likelihood surfaces are in terms of providing accurate uncertainty quantification for parameter estimation as compared to the exact or approximate likelihood. Often, methods utilizing neural networks for statistical inference focus purely on parameter point estimation as a prediction task. As such, these methods generally do not provide a measure of uncertainty with their point estimates. If shown to be reliable, confidence regions constructed from the neural likelihood provide a principled method of uncertainty quantification for parameter estimation. In Section 4, we demonstrate the reliability of these confidence regions by analyzing their empirical coverage across the parameter space Θ .

Second, these confidence regions provide a sanity check for whether the neural likelihood is an accurate representation of the exact likelihood when the exact likelihood is unavailable. If the empirical coverage for the neural likelihood surface for a sufficiently large number of realizations across the parameter space matches the expected coverage, then the neural likelihood is an accurate representation of the exact likelihood.

4 Case Studies

While our method of learning the likelihood function is applicable to any spatial process for which fast simulation is possible, we are most interested in providing inference for spatial processes with intractable likelihoods. Yet, in the intractable case, we can not directly compare the neural and exact likelihood surfaces. To address this issue, we first demonstrated that our method works as expected using a popular spatial process with a tractable likelihood, a Gaussian process, in our first case study. Additionally, since trained neural networks are fast to evaluate, we can provide a more computationally efficient way to evaluate the likelihood because computing the exact likelihood of a Gaussian process involving many spatial locations is computationally intensive. In our second case study, we applied our method to a spatial process with an intractable likelihood, a Brown–Resnick process, and compared the neural likelihood to the pairwise likelihood, a well-established approximation for the exact likelihood.

4.1 Case Study Methodology

In this section, we describe the training and evaluation details that are the same for both cases—generating training and validation data, neural network architecture, training details, calibration, and evaluation of the neural likelihood surfaces.

Input Details Since we are using a CNN as our classifier, the input shape for the spatial field and parameter must be fixed. For both processes, the spatial field is a realization $\mathbf{y} \in \mathbb{R}^{25 \times 25}$ of the spatial process for a given parameter on a 25×25 regular grid \mathcal{S} with

spatial domain $\mathcal{D} = [-10, 10] \times [-10, 10]$. For both processes, the parameter $\boldsymbol{\theta}$ is two-dimensional, and the evaluation parameter space Θ is $\Theta = (0, 2) \times (0, 2)$. The training parameter space $\tilde{\Theta}$ may differ from Θ because extending the parameter space for training the CNN can be beneficial.

Simulating Training and Validation Data To generate the training data for both spatial processes, we simulated $n = 500$ spatial field realizations for each of the $m = 3000$ parameters sampled from the training parameter space $\tilde{\Theta}$ via Latin hypercube sampling as explained in Section 3.2. Separately from the training data, we simulated $n = 500$ spatial field realizations for each of $m=300$ parameters sampled from $\tilde{\Theta}$ via Latin hypercube sampling to serve as the validation data.

Architecture Here we provide details about the CNN architecture described in Section 3.3. An ideal architecture is an architecture flexible enough to learn the likelihood for a large variety of spatial processes. To achieve such versatility, the CNN architecture must be complex enough to be able to learn a potentially rough, non-convex likelihood yet not too complex to overfit when learning a smooth, convex likelihood. While the ability to learn the likelihood for any spatial process is most likely too ambitious, the architecture we propose does have the flexibility to learn the likelihoods for both Gaussian and Brown–Resnick processes. This architecture is motivated by the architecture of the CNN trained for neural prediction in Lenzi et al. (2023).

In the first part of the architecture, there are three convolutional layers with a decreasing number of filters starting with 128 filters for the first, 128 filters for the second, and 16 for the third. All the convolutional layers have the same kernel size and activation function which are 3×3 and ReLU, respectively. Between these convolutional layers are max pooling layers with the same kernel size of 2×2 . The convolutional part outputs a flatten vector of size 64 to which we concatenate the parameter $\boldsymbol{\theta} \in \mathbb{R}^2$ resulting in a vector of size 66. In the fully connected part of the architecture, there are 4 layers with a decreasing number of neurons and the same ReLU activation function except for the last layer which has a softmax activation function to handle probabilistic binary classification. The output is a

2-d vector in which the first entry is the predicted probability $\hat{h}(\mathbf{y}, \boldsymbol{\theta}) = \hat{P}(C = 1 \mid (\mathbf{y}, \boldsymbol{\theta}))$.

Table 1: CNN architecture

layer type	output shape	filters	kernel size	activation	weights
2D convolution	[-, 23, 23, 128]	128	3×3	ReLU	1280
2D convolution	[-, 10, 10, 128]	128	3×3	ReLU	147584
2D convolution	[-, 3, 3, 16]	16	3×3	ReLU	18448
flatten and concatenate	[-, 66]				0
Dense	[-,64]			ReLU	4288
Dense	[-,16]			ReLU	1040
Dense	[-,8]			ReLU	136
Dense	[-,2]			ReLU	18

Training Details We trained the CNN for twenty epochs with different batch sizes and learning rate schedules depending on the spatial process. Depending on different batch sizes, we distributed training over four NVIDIA Tesla K80 GPUs at the most to address memory requirements for such a large matrix (i.e., batch size $\times 25 \times 25$). The batch size and learning rate schedule used for each spatial process are in Sections 4.2.2 and 4.3.2.

Calibration Our method of calibration is the same for both spatial processes; we used Platt scaling based on the regression model specified in (12). First, we generated training data by simulating $n = 50$ realizations per each of the $m = 3000$ parameters sampled via Latin hypercube sampling from the evaluation parameter space Θ . With the same process, we generated test data: $n = 50$ realizations per each of the $m = 300$ sampled parameters. The training and test data for calibration were independent of the data used to train the CNN. After constructing the two classes for both training and test data, we used the precalibrated CNN to obtain the corresponding classifier outputs. These classifier outputs coupled with the corresponding class labels formed the training and test data for the logistic regression model in (12).

To determine the effectiveness of calibration, we examined reliability diagrams as well as the neural likelihood surfaces before and after calibration for the test data. The reliability diagram depicts the empirical class probability as a function of the predicted class probability (Guo et al., 2017). For a perfectly calibrated model, the reliability diagram should show the identity function. Thus, the closer the calibrated probabilities are to the identity function, the more effective the calibration. In Sections 4.2.2 and 4.3.2, the reliability diagrams for each spatial process are displayed.

Evaluation We discuss now in detail how we evaluated the neural likelihood’s performance as compared to standard methods. First, we generated $n = 200$ spatial field realizations per parameter on a 10×10 grid over the evaluation parameter space $\Theta = (0, 2) \times (0, 2)$ for both spatial processes. We refer to these data as the evaluation data. Understanding how the neural likelihood and exact or approximate likelihood surfaces vary in behavior over Θ is important in determining whether the CNN is learning the likelihood for realizations generated from a parameter located anywhere in Θ . If there are certain regions in which the CNN underperforms, we can detect these regions when evaluating surfaces, parameter estimators, approximate confidence regions, and empirical coverage with the evaluation data.

Evaluation: Surfaces Using the process described in Section 3.5.1, we constructed the neural and exact or approximate likelihood surfaces with a 40×40 regular grid Θ^L in (13) over the evaluation parameter space $\Theta = (0, 2) \times (0, 2)$. As mentioned in Section 3.5.1, the surfaces are truly the log likelihood surfaces which ensures the ranges of the exact and neural likelihoods differ by an additive constant rather than a multiplicative constant. For visualizations, we utilized a color scale in which the maximum value of the color scale matches the maximum value of the particular surface to deal with the shifted range due to the additive constant for the neural likelihood surface. We selected a range of ten units for the color scale because an approximate confidence region in a two-dimensional parameter space has 99% coverage probability for a cut-off value of $C_{.01} = 9.21$, the 99% quantile of a Chi distribution with two degrees of freedom in (18).

Evaluation: Parameter Estimation To compare the parameter estimates for neural and exact or approximate likelihood, we display a 4×4 grid of plots in which each plot contains the parameter estimates for both methods, neural and exact or approximate likelihood, for 200 realizations generated from a single parameter in the evaluation data. The parameter estimates for the neural likelihood before and after calibration are the same because Platt scaling is a monotonic transformation. Since the parameter estimates are all on the same 40×40 grid, the estimates are jittered with a small amount of noise in Figure 6 to distinguish individual estimates. The parameters which generate the realizations range from 0.4 to 1.6 by increments of 0.4 for both parameters.

Evaluation: Approximate Confidence Regions We constructed 95% approximate confidence regions for each realization in the evaluation data. For both spatial processes, calibration increases the size while preserving the shape and location of the neural likelihood confidence region because Platt scaling is a monotonic transformation.

Evaluation: Empirical Coverage and Confidence Region Area We computed empirical coverage and confidence region area for the evaluation data. For each of the two hundred realizations $\{\mathbf{y}_{j,l}\}_{j \in [200]}$ per parameter $\boldsymbol{\theta}_l$ on the 10×10 grid, we determined whether the true parameter $\boldsymbol{\theta}_l$ is in the 95% approximate confidence region as well as the area of the region. The empirical coverage for the parameter $\boldsymbol{\theta}_l$ is

$$\frac{1}{n} \sum_{j=1}^n \mathbf{1}(\boldsymbol{\theta}_l \in \mathcal{C}_{\text{NN},95}(\Theta^L, \mathbf{y}_{j,l})). \quad (21)$$

where $n = 200$. We visualize the empirical coverage and confidence region area with a heat map over the evaluation parameter space Θ to determine whether the coverage and area vary over Θ . For both spatial processes, empirical coverage for neural likelihood increases after calibration due to the increase in size of the confidence regions.

Evaluation: Timing Study To compare the computational requirements of neural and exact or approximate likelihood, we conducted a timing study for evaluating surfaces using an Intel Core i7-10875H processor with eight cores, each with two threads. For fifty

realizations $\mathbf{y}_i \in \mathbb{R}^{25 \times 25}$, we recorded the average elapsed time and standard deviation in evaluating the neural likelihood surface on a 40×40 grid over the evaluation parameter space Θ . As discussed in Section 3.5.1, the CNN can handle vectorized inputs which significantly accelerates evaluation of the neural likelihood surface. To understand the impact of vectorization, we timed the evaluation of the neural likelihood when using both vectorized and unvectorized inputs.

We repeated a similar study for the exact or approximate likelihood using the same fifty realizations $\mathbf{y}_i \in \mathbb{R}^{25 \times 25}$ for Gaussian and Brown–Resnick processes respectively. As far as we are aware, there is no prepackaged way to vectorize the evaluation of these exact and approximate likelihoods. Due to this discrepancy in the ability to handle vectorized computations, the time difference between constructing the neural and the exact or approximate likelihood surfaces is significant as shown in Sections 4.2.2 and 4.3.2.

Evaluation: Multiple Realizations As explained in Section 3.1, our method of learning the likelihood is applicable to the case of an arbitrary number of i.i.d. realizations $\mathbf{y}_1 \dots \mathbf{y}_n$ from the spatial process without needing to retrain the single-realization neural network. To demonstrate this, we generated evaluation data for five i.i.d. spatial field realizations in the same manner as we did in the single realization case and evaluated neural likelihood according to (8) for the evaluation data. We display the 4×4 plot of the resulting parameter estimates as we do for the single realization case.

4.2 First Case Study: Gaussian Process with Computationally Intensive Likelihood

We first applied our method to a Gaussian process because this popular stochastic process has a tractable exact likelihood to which we can compare the neural likelihood. The primary purpose of this case study is to validate our method in a case where the exact likelihood is available. A secondary purpose of this case study is demonstrating the computational benefits of our method. Gaussian processes are often used to model spatial data, yet they are computationally costly due to a matrix inversion necessary to compute the likelihood.

For a Gaussian process evaluated at n locations, the time complexity is approximately $\mathcal{O}(n^3)$ depending on the algorithm as well as other factors (Sun et al., 2012). As n grows, this matrix inversion quickly becomes impractical. As such, developing a more computationally efficient method that provides a comparable quality of parameter estimation and uncertainty quantification as exact likelihood is an important issue in of itself. As shown in this section, our method of learning the likelihood provides one approach.

4.2.1 Description of Gaussian Process and Its Exact likelihood

We applied our method to a Gaussian process with a zero mean function and an exponential covariance function with two positive parameters—length scale ℓ and variance ν . Hence, the model is

$$f \sim \text{GP}(m(\mathbf{x}), k(\mathbf{x}, \mathbf{x}')), \text{ where } m(\mathbf{x}) = 0 \text{ and } k(\mathbf{x}, \mathbf{x}') = \nu \exp\left(-\frac{\|\mathbf{x} - \mathbf{x}'\|_2}{\ell}\right). \quad (22)$$

For a realization $\mathbf{y} = f(\mathcal{S})$, where \mathcal{S} is a regular finite grid \mathcal{S} of s locations with covariance matrix $\Sigma = (k(\mathbf{x}_i, \mathbf{x}_j))_{i,j} \in \mathbb{R}^{s \times s}$, the log likelihood is

$$\log(\mathcal{L}(\boldsymbol{\theta} \mid \mathbf{y})) = -\frac{1}{2} \mathbf{y}^\top \Sigma^{-1} \mathbf{y} - \frac{s}{2} \log(2\pi) - \frac{1}{2} \log(\det(\Sigma)) \quad (23)$$

where $\boldsymbol{\theta} = (\nu, \ell)$ (Rasmussen and Williams, 2006, 81-96).

The two most computationally intensive operations in (23) are computing the inverse and the determinant of the covariance matrix Σ each with a time complexity of $\mathcal{O}(s^3)$. To efficiently compute both of these operations, we utilized the Cholesky decomposition of the symmetric, positive-definite matrix Σ ,

$$\Sigma = \mathbf{L}\mathbf{L}^\top, \quad (24)$$

where $\mathbf{L} \in \mathbb{R}^{s \times s}$ is a lower triangular matrix (Rasmussen and Williams, 2006, 202-203). While Cholesky decomposition is computationally expensive with a time complexity of $\mathcal{O}(s^3)$, substituting the Cholesky decomposition for the covariance matrix reduces the number of $\mathcal{O}(s^3)$ operations from two to one.

4.2.2 Experiments

Training and Model Selection The training parameter space $\tilde{\Theta}$ was extended beyond the evaluation parameter space Θ to $\tilde{\Theta} = (0, 2.5) \times (0, 2.5)$ to better learn the likelihood and prevent potential biases at the boundary. We trained several models with varying configurations of batch size and learning rate schedule. We selected a model with the lowest validation loss amongst the versions in which there was little to no indication of overfitting in the plot of training and validation loss. The selected model was trained with a batch size of 30000 and a learning rate schedule in which the learning rate started at 0.001 for the first five epochs and decreased by a multiplicative factor of $e^{-0.1}$ for each epoch after the first five.

When experimenting with different batch sizes and learning rate schedules, we observed that as batch size decreases, overfitting tends to increase for a fixed learning rate schedule. Decreasing initial learning rate reduces but does not eliminate overfitting. We did not observe a similar tendency for overfitting during training for the Brown–Resnick process and speculate that the CNN architecture might be too complex for learning the relatively simple likelihood of a Gaussian process unless care is taken when selecting batch size and learning rate schedule.

Calibration The reliability diagrams before and after calibration in Figure 4 show great improvement in how closely the predicted class probabilities match the true class probabilities. Before calibration, the empirical probability for class one is generally higher than expected for any given predicted probability for class one. Calibration fixes this tendency for the classifier to underestimate the probability a given realization and parameter is in the first class, the class in which the parameter θ and spatial field realization \mathbf{y} are dependent. Since learning the likelihood relies on estimating the class probability correctly, fixing this tendency produces calibrated neural likelihood surfaces in which the area of high likelihood is larger and improves approximate confidence regions and empirical coverage as we demonstrate later in this section.

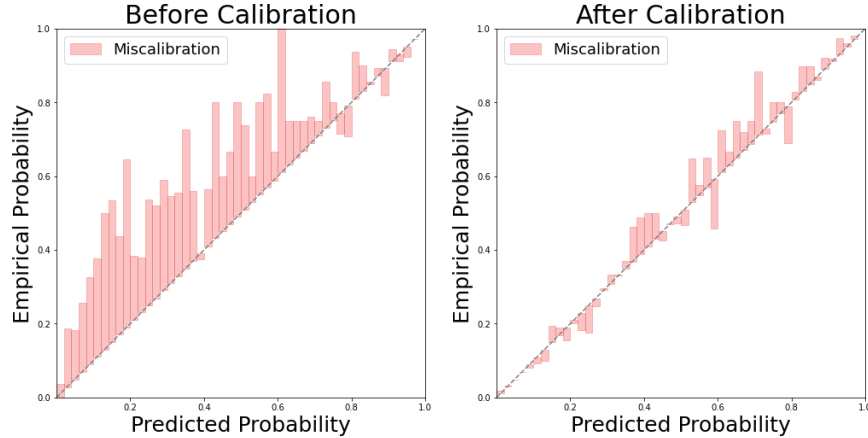


Figure 4: Reliability diagram for class one before calibration (left) and after calibration (right) for Gaussian process.

Surfaces We compared the neural likelihood surface before and after calibration to the exact likelihood surface for the same realization \mathbf{y} in the evaluation data. Across the evaluation parameter space Θ , the area of high likelihood for the neural likelihood surfaces are similar in shape and location to the corresponding exact likelihood surfaces yet differ in size. In correcting the classifier’s tendency to underestimate the predicted probability for class one, calibration spreads out the region of high likelihood. Consequentially, the neural likelihood surfaces more closely resemble the exact likelihood surfaces in terms of the size of the region of greatest likelihood. Yet, the area of high likelihood is slightly too large in the calibrated neural likelihood surfaces. We observed this pattern of calibrated neural likelihood surfaces more closely resembling exact likelihood surfaces for spatial field realizations generated from any parameter across Θ .

Parameter Estimation We compare the exact and neural likelihood parameter estimates using the 4×4 grid of plots described in Section 4.1. From Figure 6, we conclude that the parameter estimates for both methods are comparable across the evaluation parameter space Θ . This indicates that the neural likelihood serves as a great surrogate for the exact likelihood in terms of point estimation. The neural likelihood estimator $\hat{\boldsymbol{\theta}}_{NN}$ has greater variance than the exact likelihood estimator $\hat{\boldsymbol{\theta}}$, yet the patterns of behavior are the same for both estimators across Θ . For instance, as the true length scale ℓ increases, both

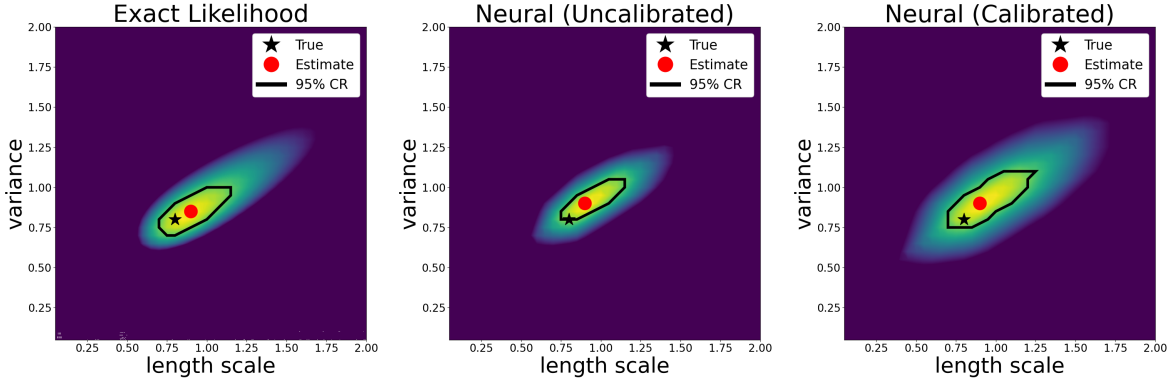


Figure 5: Surfaces for exact log exact likelihood (left), neural likelihood before calibration (center), and neural likelihood after calibration (right) for a realization of a Gaussian process with parameters $\nu = 0.8$ and $\lambda = 0.8$. In each figure, the color scale ranges from the maximum value of the surface to ten units less than the maximum value.

exact and neural likelihood estimators increase in variance along the length scale axis.

Approximate Confidence Regions As shown in Figure 5, the neural likelihood approximate confidence regions become larger and more similar to the exact likelihood approximate confidence regions after calibration. In general, the shapes and locations of the confidence regions for the exact and uncalibrated neural likelihood surfaces are similar yet the sizes are not. After calibration, the neural and exact likelihood confidence regions become more comparable in size because the neural likelihood confidence regions increase in size from 60% to 120% of the size of the exact likelihood confidence regions on average.

Empirical Coverage and Confidence Region Area In Figure 7, empirical coverage of the 95% approximate confidence regions for both neural and exact likelihood is essentially uniform and approximately 95% across the evaluation parameter space Θ . Thus, there are not regions of Θ for which the exact and neural likelihood surfaces suffer in terms of accuracy.

As shown in Figure 8, calibration increases average confidence region area for neural likelihood from 60% to 120% of the average area for exact likelihood. Confidence region area for exact and neural likelihood become more comparable after calibration, and thus,

Neural vs Exact Likelihood Estimates

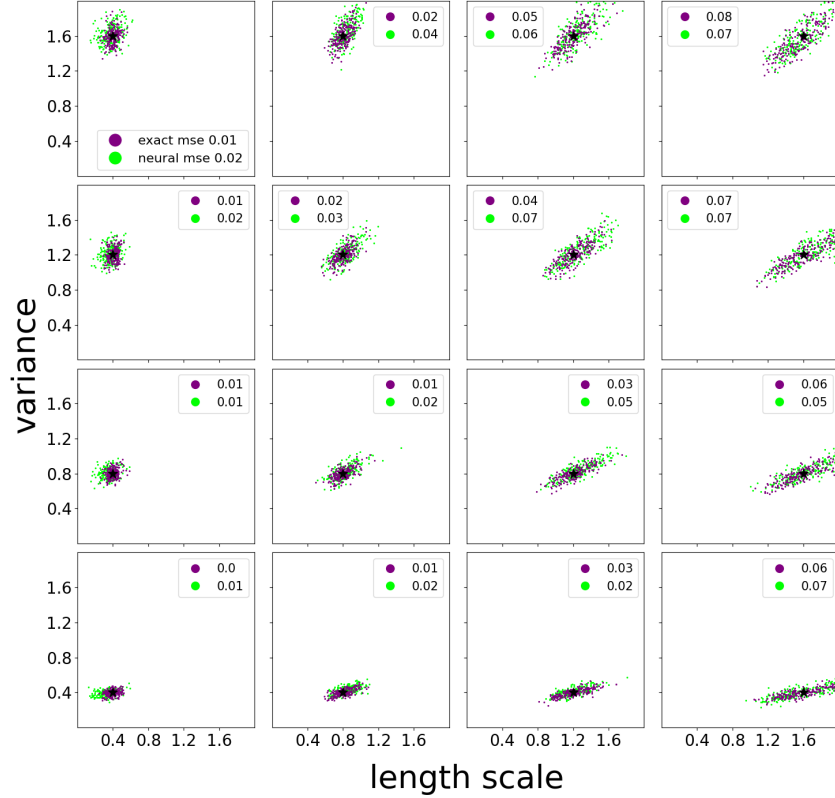


Figure 6: Parameter estimates for exact and neural likelihood for a Gaussian process. Each of the 16 plots contains the true parameter (black cross) which generated the 200 spatial field realizations and the corresponding parameter estimates for exact likelihood (purple) and neural likelihood (green) with mean squared error (MSE) in the legend. The true parameter increases in variance from bottom to top and in length scale from left to right.

empirical coverage for neural likelihood increases from 80% to approximately 94% across Θ .

Timing Study For the timing study, the exact likelihood surfaces were constructed using Cholesky factorization and multicore processing to both accelerate the process and utilize the full resources of the processor. There are two methods to construct the neural likelihood surfaces—unvectorized and vectorized. The unvectorized method involves evaluation of the neural network separately at each parameter on the 40×40 grid. In contrast, the vectorized method takes advantage of a neural network’s ability to quickly evaluate multiple inputs

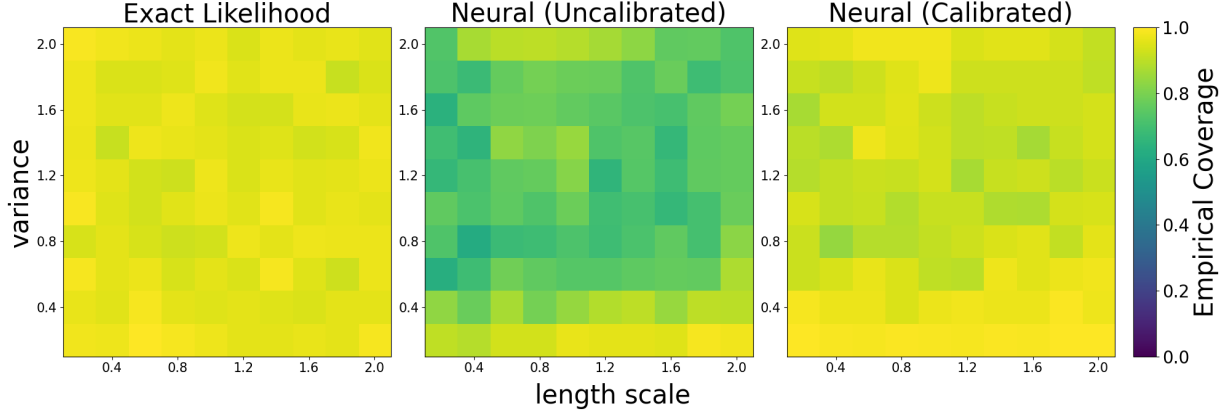


Figure 7: Empirical coverage for 95% approximate confidence regions for the exact likelihood (left) and neural likelihood before calibration (center) and after calibration (right) for 200 realizations per parameter on a 10×10 grid over Θ .

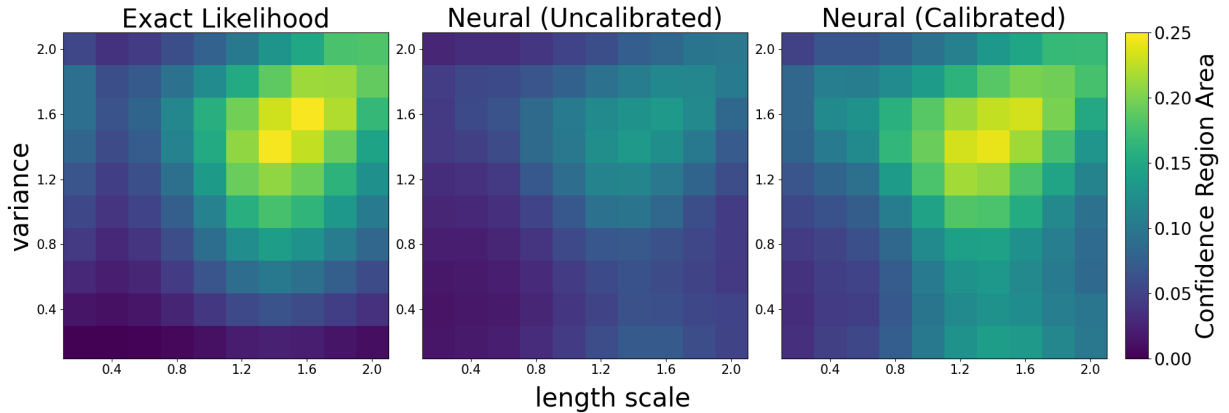


Figure 8: 95% approximate confidence region area for exact likelihood (left) and neural likelihood before calibration (center) and after calibration (right) for 200 realizations per parameter on a 10×10 grid over Θ .

at once. We refer the reader to Section 3.5.1 for details.

As shown in Table 2, the vectorized method of producing neural likelihood surfaces is significantly faster than the unvectorized method by a factor of approximately 6. The neural likelihood surfaces produced via the vectorized method are approximately thirty times faster to produce than exact likelihood surfaces. Since computation of exact likelihood increases cubically with the number of spatial locations, we expect that the vectorized method

Table 2: Time to produce neural and exact likelihood surfaces on a 40×40 grid over Θ for 50 realizations of a Gaussian process on a 25×25 grid with a spatial domain of $[-10, 10] \times [-10, 10]$.

Type of Surface and Method	average (sec)	standard deviation (sec)
exact likelihood	71.67	1.02
unvectorized neural likelihood	13.46	.26
vectorized neural likelihood	2.26	.34

of producing the neural likelihood surface will only increase in computational efficiency in comparison to exact likelihood as the number of spatial locations increases.

Multiple Realizations The parameter estimators for both the exact and neural likelihood for the five i.i.d. realizations case in Figure 9 are more accurate and have less variance than equivalent estimators for the single realization case in Figure 6, as expected. As in the single realization case, the neural likelihood estimator $\hat{\theta}_{NN}$ has slightly greater variance than the exact likelihood estimator $\hat{\theta}$, yet the patterns of behavior are similar for both estimators across the evaluation parameter space Θ .

Summary of Results From this case study, we demonstrated that our method of learning the likelihood is both accurate and computationally efficient for Gaussian processes. Once calibrated, the neural and exact likelihood surfaces, parameter estimates, and approximate confidence regions are comparable. From the evaluation of neural likelihood surfaces, confidence regions, and empirical coverage before after calibration, it is clear that calibration is essential to our method in order to achieve results comparable to exact likelihood. Finally, the calibrated neural likelihood surfaces are significantly faster to evaluate than exact likelihood surfaces because neural networks are fast to evaluate and our CNN, once trained, is amortized. Thus, we have both validated our method in a case where the exact likelihood is available and shown this method is more computationally efficient than exact likelihood.

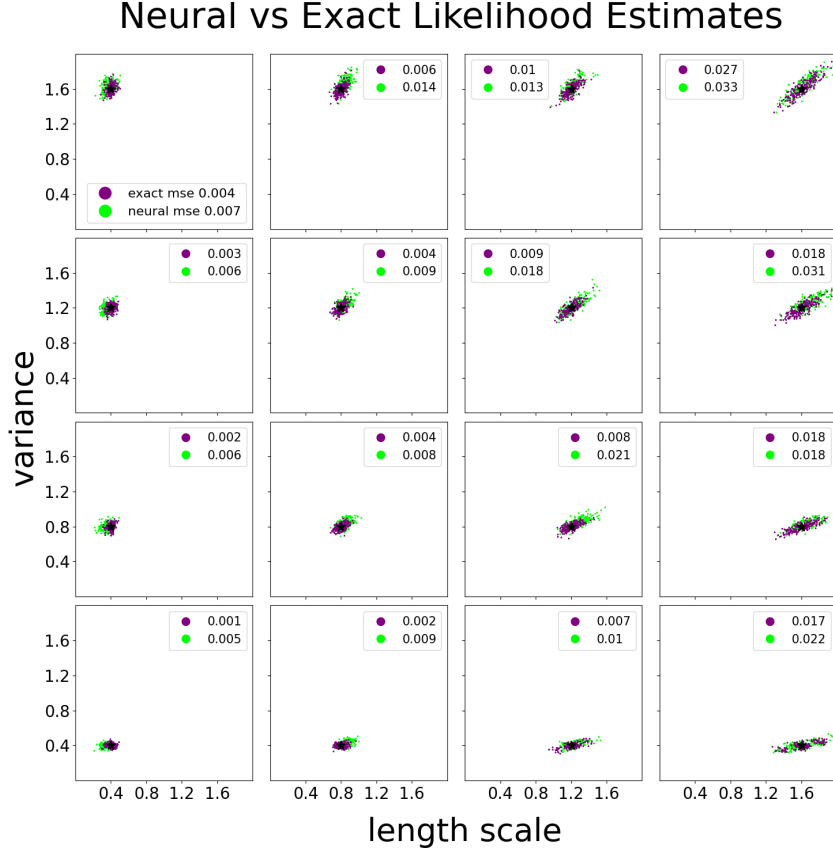


Figure 9: Parameter estimates for exact and neural likelihood in the case of 5 i.i.d. spatial field realizations for a Gaussian process. Each of the 16 plots contains the true parameter (black cross) which generated the realizations and the corresponding parameter estimates for exact likelihood (purple) and neural likelihood (green) with mean squared error (MSE) in the legend. The true parameter increases in variance from bottom to top and in length scale from left to right.

4.3 Second Case Study: Brown–Resnick Process with an Intractable Likelihood

We next applied our method to the Brown–Resnick process which has an intractable likelihood function; yet the process also has an approximation for the exact likelihood called composite likelihood (Castruccio et al., 2016) to which we can compare the neural likelihood. The Brown–Resnick process is a stochastic process belonging to a family of max-stable processes which are often used to model spatial extremes (Davison et al., 2012). Our selection of a Brown–Resnick Process for this case study is in part due to the use of this

process as a proof of concept for neural prediction in Lenzi et al. (2023).

4.3.1 Description of Brown–Resnick Process and its Approximate Likelihood

In general, we can construct a max-stable process from other stochastic processes in the following way. First, consider the points η_i of a positive Poisson point process with intensity function $d\Lambda(\eta) = \eta^{-2} d\eta$ and i.i.d. realizations $W_i(\mathbf{s})$ of a non-negative stochastic process with a mean of one. For independent realizations of the Poisson process and the non-negative process, a max-stable process has the following form:

$$Z(\mathbf{s}) = \max_{i>0} \eta_i W_i(\mathbf{s}) \text{ for a location } \mathbf{s} \text{ on a domain } \mathcal{D} \subset \mathbb{R}^d \quad (25)$$

with marginal $P(Z(\mathbf{s}) \leq z) = \exp(-\frac{1}{z})$, the unit Fréchet distribution (Kabluchko et al., 2009).

Depending on what non-negative stochastic process we select for $W_i(\mathbf{s})$, we obtain different max-stable processes (Kabluchko et al., 2009). We can construct the Brown–Resnick process using (25) with $W_i(\mathbf{s}) = \exp(\epsilon_i(\mathbf{s}) - \gamma(\mathbf{s}))$, where $\epsilon_i(\mathbf{s})$ are realizations of an intrinsically stationary Gaussian process such that $\epsilon_i(\mathbf{s}) = 0$ almost surely with semivariogram $\gamma(\mathbf{h}) = (\frac{\|\mathbf{h}\|}{\lambda})^\nu$ where \mathbf{h} is the spatial separation between two locations, $\lambda \in \mathbb{R}^+$ is a range parameter, and $\nu \in (0, 2]$ is a smoothness parameter (Castruccio et al., 2016). As such, the parameter space Θ for which we are interested in learning the likelihood is a bounded subset of $\mathbb{R}^+ \times (0, 2]$.

The density is

$$f(z_1, \dots, z_n) = \exp(-V(z_1, \dots, z_n)) \sum_{\mathcal{P} \in \mathcal{P}_z} \prod_{S \in \mathcal{P}} -V_S(z_1, \dots, z_n) \quad (26)$$

where \mathcal{P}_z is the set of all partitions \mathcal{P} of the values z_1, \dots, z_n and V_S is the partial derivative of

$$V(z_1, \dots, z_n) = E(\max\{\frac{W(\mathbf{s}_1)}{z_1}, \dots, \frac{W(\mathbf{s}_n)}{z_n}\}) \quad (27)$$

with respect to the values z_1, \dots, z_n indexed by $S \in \mathcal{P}$ (Castruccio et al., 2016; Huser and Davison, 2013). The number of terms in the summation in (26) is $|\mathcal{P}_z| = B_n$, the Bell number for n , which grows more than exponentially (Castruccio et al., 2016).

Since the number of spatial locations is generally large in practice, the computation of the likelihood for a Brown–Resnick process is intractable in many practical cases. Yet, in the bivariate case of only two spatial locations, the likelihood has a simple closed form. From (26), the bivariate log likelihood is

$$\ell(\lambda, \nu) = \log \left(V_1(z_1, z_2)V_2(z_1, z_2) - V_{12}(z_1, z_2) \right) - V(z_1, z_2) \quad (28)$$

in which V and its partial derivatives V_1, V_2 and V_{12} are tractable (Huser and Davison, 2013). Using the bivariate case of the full likelihood, we can provide an approximation for the full likelihood of a Brown–Resnick process called pairwise likelihood, a form of composite likelihood. (Padoan et al., 2010).

In pairwise log likelihood, the summands are the bivariate likelihoods between two spatial locations \mathbf{s}_{j_1} and \mathbf{s}_{j_2} for $j_1, j_2 \in [n]$, and involve only select pairs of spatial locations $(\mathbf{s}_{j_1}, \mathbf{s}_{j_2})$ because even a summation over all $\frac{n(n-1)}{2}$ pairs of spatial locations is computationally intensive for a large number of spatial locations. The pairwise log likelihood has the following form (Huser and Davison, 2013; Castruccio et al., 2016):

$$\log \left(\mathcal{L}_{\text{approx}}((\lambda, \nu) \mid \mathbf{z}) \right) = \sum_{j_2 > j_1} \sum_{j_1=1}^n w_{j_1, j_2} \log \left(V_1(z_{j_1}, z_{j_2})V_2(z_{j_1}, z_{j_2}) - V_{12}(z_{j_1}, z_{j_2}) \right) - V(z_{j_1}, z_{j_2}) \quad (29)$$

where the weights w_{j_1, j_2} are between zero and one depending on whether the bivariate likelihood for the pair of spatial locations $(\mathbf{s}_{j_1}, \mathbf{s}_{j_2})$ is included in the summation. Inclusion is based on a criterion such as the following:

$$w_{j_1, j_2} = \begin{cases} 1, & \text{if } \|\mathbf{s}_{j_1} - \mathbf{s}_{j_2}\| \leq \delta, \\ 0, & \text{otherwise.} \end{cases} \quad (30)$$

Since nearby locations contain the most information about a given location, the selection criterion generally is determined by the distance between spatial locations. In (30), all pairs of observations whose locations are within a certain cut-off distance δ of each other are included.

When computing the pairwise likelihood, the cut-off distance δ is a tuning parameter which must be appropriately selected in order to obtain reasonable results. In practice, if

the cut-off distance is too small or too large, the maximum pairwise likelihood estimates are highly inaccurate, and the pairwise likelihood surfaces are uninformative as shown in Section 4.3.2. In Section 4.3.2, we construct pairwise likelihood surfaces and estimates using various cut-off values δ and compare the results against those obtained using neural likelihood which does not involve such tuning parameters.

4.3.2 Experiments

Training and Model Selection We had some difficulty training the CNN for various combinations of learning rate schedule and batch size. The training and validation loss would generally plateau after a few epochs. Simply training the CNN with the same batch size and learning rate schedule for various initializations of the weights eventually produced a model in which the training and validation loss did not plateau early in training. The selected model for which plateauing did not occur was trained using a batch size of 50 and a learning rate schedule in which the learning rate started at 0.002 for the first five epochs and decreased by a multiplicative factor of $e^{-0.1}$ for each epoch after the first five.

We experimented with a training parameter space $\tilde{\Theta} = (0, 2) \times (0, 2.5)$ in which the domain of the smoothness parameter ν is not extended because this parameter is bounded from zero to two as described in Section 4.3.1. Yet, extending $\tilde{\Theta}$ beyond the evaluation parameter space Θ caused problems during training. The validation loss fluctuated while the training loss smoothly decreased as the number of epochs increased. In contrast, the validation loss smoothly decreased with the training loss for the CNN trained on data from $\Theta = (0, 2) \times (0, 2)$. Thus, the model we selected was trained on data from the training parameter space $\tilde{\Theta} = (0, 2) \times (0, 2) = \Theta$ with the batch size and learning rate schedule described earlier.

Calibration The reliability diagrams before and after calibration in Figure 10 show great improvement in how closely the predicted class probabilities match the true class probabilities after calibration. Before calibration, the classifier either underestimates or overestimates the probability of a given parameter and spatial field pair belonging to class one depending on the predicted class one probability. Calibration, by and large, fixes these ten-

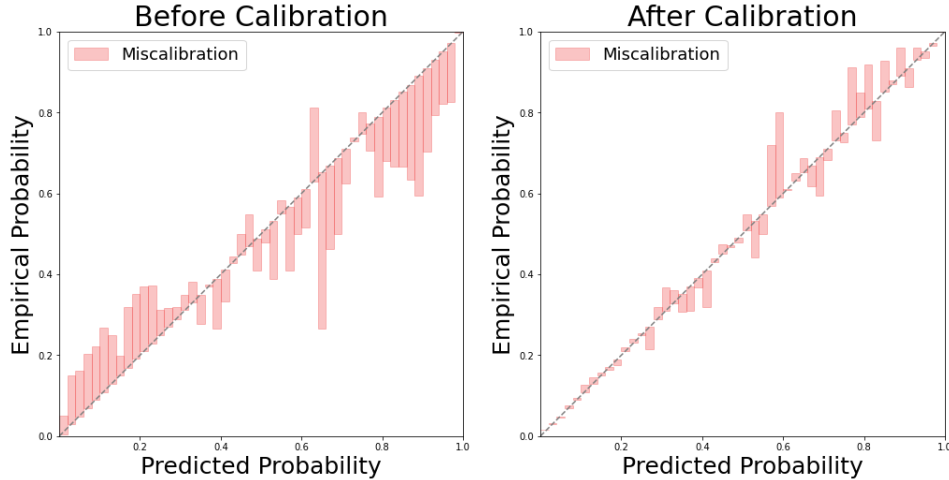


Figure 10: Reliability diagrams for class one before calibration (left) and after calibration (right) for Brown–Resnick process.

dencies, and the resulting calibrated neural likelihood surfaces and approximate confidence regions are more accurate as we demonstrate later in this section.

Pairwise Likelihood We compare neural likelihood to pairwise likelihood for various cut-off distances δ . To compute pairwise likelihood, we used the weighting scheme in (30) with varying cut-off distances δ and the `fitmaxstab` function in the R package `SpatialExtremes` (Ribatet, 2020). The `fitmaxstab` function fits data to a max-stable process such as a Brown–Resnick process and returns a list of objects including the function `nllh`, the negative log pairwise likelihood function for the given data and weighting scheme. For each realization \mathbf{y} in the evaluation data, we produced a pairwise likelihood surface, parameter point estimate and approximate confidence region by evaluating the `nllh` function at each parameter on the 40×40 grid over the evaluation parameter space Θ .

Surfaces We compare the neural likelihood surface before and after calibration to the pairwise likelihood surface for various distance cut-offs δ for the same realization \mathbf{y} in the evaluation data in Figure 11. We do not expect the neural and pairwise likelihood surfaces to exactly mirror each other because pairwise likelihood is an approximation of the exact likelihood. In general, the area of high likelihood in the pairwise surface becomes smaller

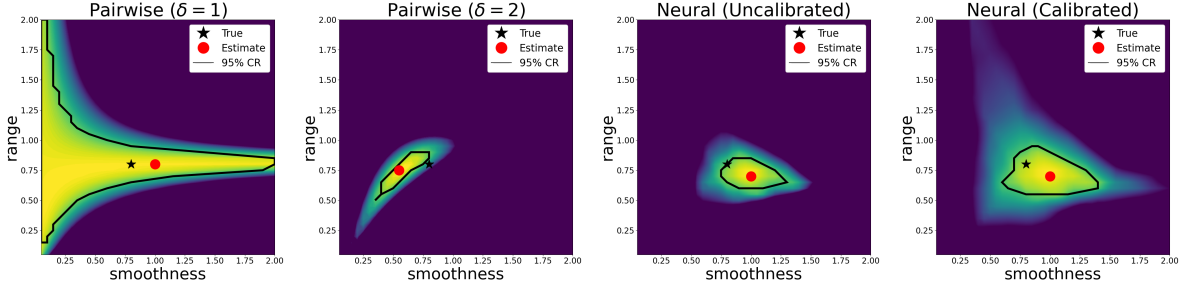


Figure 11: The pairwise likelihood surface for a distance cut-off $\delta = 1$ (far left) and $\delta = 2$ (center left) and neural likelihood surface before calibration (center right) and after calibration (far right) for a realization of a Brown–Resnick process with parameters $\nu = 0.8$ and $\lambda = 0.8$. In each figure, the color scale ranges from the maximum value of the surface to ten units less than the maximum value.

as the cut-off δ increases indicating that the pairwise likelihood surface is highly sensitive to the choice of δ . The neural and pairwise likelihood surfaces for any cut-off exhibit very different behavior in shape, location, and size of the area of high likelihood. Calibration increases the area but maintains the shape and location of the high likelihood region in the neural likelihood surface.

Parameter Estimation As described in Section 3.5.2, the parameter estimate is the parameter on the grid Θ^L which maximizes the given surface. In Figure 12, we compare parameter estimates for neural and pairwise likelihood for cut-off $\delta = 2$, the optimal cut-off in terms of parameter estimation. To determine the optimal cut-off, we varied δ and observed that the accuracy of pairwise estimates increases as δ increases from 0 to approximately 2 and then decreases as δ increases beyond 2. See Figure 15 in Section 6 for pairwise estimates with different cut-offs δ . From Figure 12, we observe that the neural and pairwise estimates are similar in terms of accuracy and behavior except in certain areas of the evaluation parameter space Θ . For large smoothness and small range, the pairwise estimates are significantly more accurate than the neural estimates because the pairwise estimates are less biased and have less variance. For small smoothness and large range, the neural estimates are slightly more accurate than the pairwise estimates.

Neural vs Pairwise ($\delta = 2$) Parameter Estimates

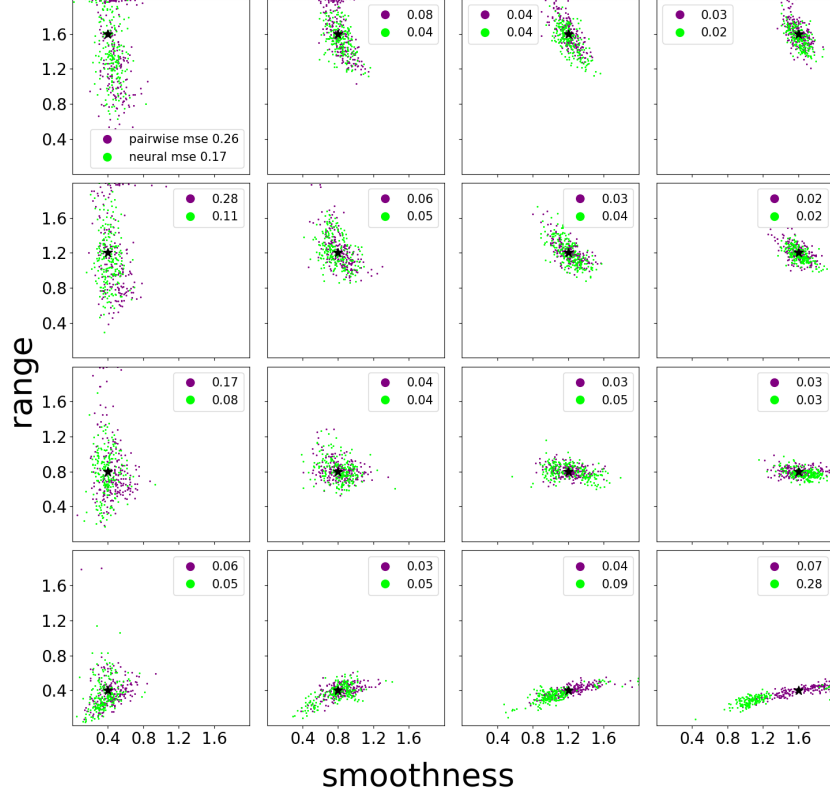


Figure 12: Parameter estimates for neural likelihood and pairwise likelihood with $\delta = 2$. Each of the 16 plots contains the true parameter (black cross) which generated the 200 spatial field realizations and the corresponding parameter estimates for pairwise likelihood (purple) and neural likelihood (green) with mean squared error (MSE) in the legend. The true parameter increases in range from bottom to top and in smoothness from left to right.

Approximate Confidence Regions As shown in Figure 11, the approximate confidence regions for pairwise likelihood shrink rapidly in size and change shape as the distance cut-off δ increases. The neural and pairwise confidence regions have remarkably different shapes and sizes no matter the cut-off value. After calibration, the neural confidence regions become larger in size yet retain their shape and location.

Empirical Coverage and Confidence Region Area As the distance cut-off δ increases, confidence region area and thus empirical coverage decrease for the 95% approximate confidence regions constructed from pairwise likelihood surfaces as shown in Figures 14

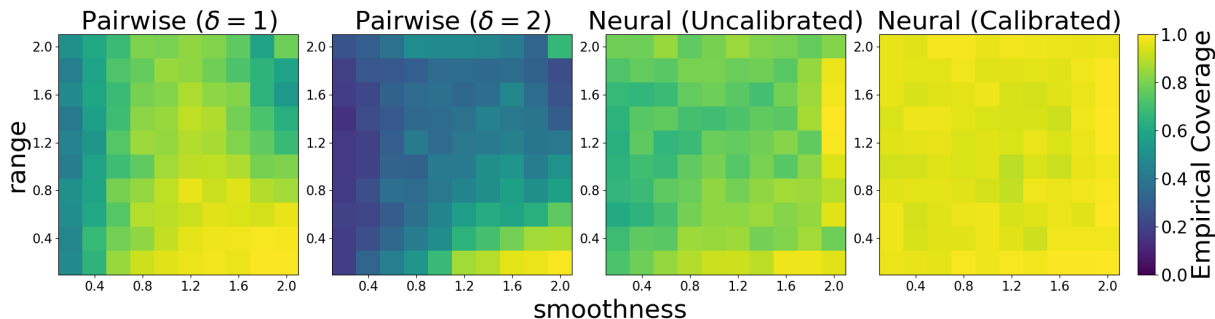


Figure 13: Empirical coverage for 95% approximate confidence regions for pairwise likelihood with distance cut-off $\delta = 1$ (far left) and $\delta = 2$ (center left) and neural likelihood before calibration (center right) and after calibration (far right).

and 13 respectively. For distance cut-off $\delta = 1$, empirical coverage is high due to the large, impractical confidence regions constructed from these surfaces. For distance cut-off $\delta = 2$, the confidence regions are unrealistically, small, and thus, empirical coverage is low.

As in the Gaussian process case, calibration increases confidence region area for the neural likelihood and thus increases empirical coverage close to the intended 95% coverage. Empirical coverage for neural likelihood is uniform over the evaluation parameter space Θ whereas empirical coverage for pairwise likelihood varies. This observation indicates that pairwise likelihood suffers in particular for some regions of Θ while neural likelihood has no such regions of significantly worse coverage. To conclude, neural likelihood provides better empirical coverage than pairwise likelihood for distance cut-off $\delta = 1, 2$ while keeping confidence region area relatively small and coverage across Θ relatively uniform.

Timing Study To produce pairwise likelihood surfaces for the timing study, we first extracted the pairwise likelihood function called `nllh` from the `fitmaxstab` function in the `SpatialExtremes` R package (Ribatet, 2020). Since the `fitmaxstab` function involves finding the parameters that best fit the spatial field via L-BFGS, we limited the number of optimization iterations to zero in order to only count the time necessary to construct the likelihood surface. Finally, we used parallel processing with 8 cores, each with 2 threads, to evaluate the pairwise likelihood function `nllh` at each parameter of the 40×40 grid over the evaluation parameter space Θ .

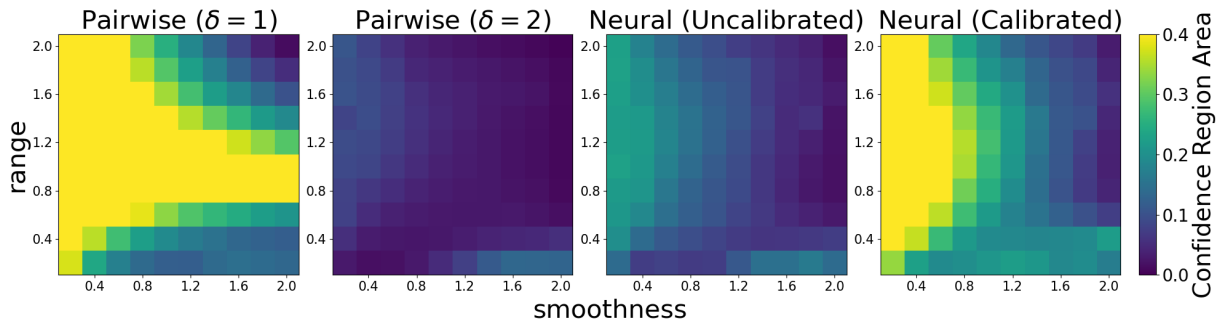


Figure 14: 95% approximate confidence region area for pairwise likelihood with a distance cut-off of $\delta = 1$ (far left) and $\delta = 2$ (center left) and neural likelihood before calibration (center right) and after calibration (far right).

Table 3: Time to produce neural and pairwise likelihood surfaces on a 40×40 grid over Θ for 50 realizations of a Brown–Resnick process on a 25×25 grid on spatial domain $[-10, 10] \times [-10, 10]$.

Type of Surface and Method	average (sec)	standard deviation (sec)
pairwise likelihood ($\delta = 1$)	5.05	0.34
pairwise likelihood ($\delta = 2$)	5.38	0.27
pairwise likelihood ($\delta = 5$)	5.86	0.28
pairwise likelihood ($\delta = 10$)	7.33	0.16
vectorized neural likelihood	2.24	0.13
unvectorized neural likelihood	14.39	0.03

As the distance cut-off δ increases, the time to construct the corresponding pairwise likelihood surface should increase because the number of spatial location pairs for which the bivariate likelihood is computed increases. As expected, the time to compute the pairwise likelihood surface does increase, yet only slightly, as the distance cut-off δ increases as seen in Table 3. Depending on the distance cut-off δ , the vectorized method of producing the neural likelihood surface is approximately two to three times faster than pairwise likelihood. However, the unvectorized method is at least twice as slow as computing the pairwise likelihood surface. Thus, the efficiency of neural likelihood surfaces is due to the ability to evaluate the CNN at multiple inputs simultaneously.

Multiple Realizations The parameter estimators for both pairwise and neural likelihood for the five i.i.d. realizations case in Figure 15 are more accurate and have less variance than equivalent estimators for the single realization case in Figure 12, as expected. As in the single realization case, the neural and pairwise estimates are similar in terms of accuracy and behavior except in certain areas of the evaluation parameter space Θ . For large smoothness and small range, the pairwise estimates are significantly more accurate than the neural estimates. Yet, for small smoothness and large range, the neural estimates are slightly more accurate than the pairwise estimates.

Summary of Results From this case study, we demonstrated that our method of learning the likelihood is more accurate in terms of parameter estimation and uncertainty quantification than pairwise likelihood, a well-established approximation for the intractable exact likelihood. The neural likelihood parameter estimates are comparable or significantly better than the pairwise likelihood parameter estimates depending on the distance cut-off δ . The approximate confidence regions for neural likelihood provide better uncertainty quantification than pairwise likelihood: the neural confidence regions achieve empirical coverage comparable to the intended coverage with a sufficiently small confidence region area. From the evaluation of neural likelihood surfaces, confidence regions, and empirical coverage before and after calibration, it is clear that calibration is essential to our method in order to achieve the intended coverage level of the approximate confidence regions. Finally, the neural likelihood surfaces are significantly faster to evaluate than pairwise likelihood surfaces because neural networks are fast to evaluate and our CNN, once trained, is amortized.

5 Discussion and Conclusions

In this paper, we have proposed a new method to learn the likelihood function of spatial processes using a specifically designed classification task. This classification task involves generating simulated data from the spatial process to construct two classes which consist of pairs of dependent and independent spatial fields \mathbf{y} and parameters $\boldsymbol{\theta}$. Due to the construction of the classes, the resulting classifier is equivalent to the likelihood up to a

Neural vs Pairwise ($\delta = 2$) Parameter Estimates

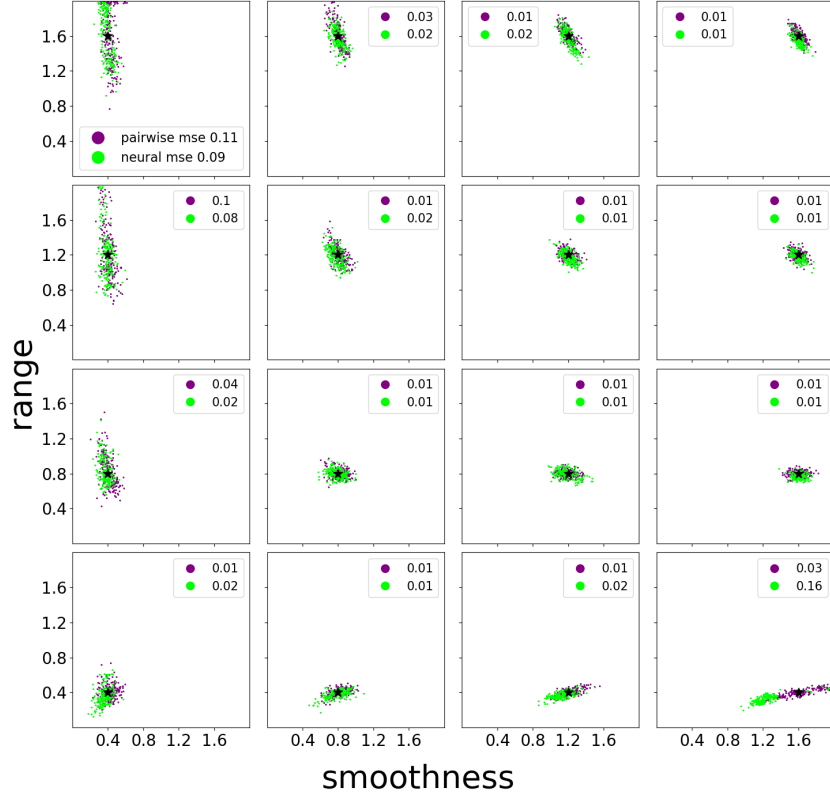


Figure 15: Parameter estimates for neural likelihood and pairwise likelihood with $\delta = 2$ in the case of 5 i.i.d. spatial field realizations for a Brown–Resnick process. Each of the 16 plots contains the true parameter (black cross) which generated the realizations and the corresponding parameter estimates for pairwise likelihood (purple) and neural likelihood (green) with mean squared error (MSE) in the legend. The true parameter increases in range from bottom to top and in smoothness from left to right.

multiplicative constant and a known transformation. Once we calibrate the classifier, we can transform the classifier outputs to produce neural likelihood surfaces, approximate confidence regions, and parameter estimates.

We demonstrated that the neural likelihood produces comparable results to the exact likelihood in terms of parameter estimation and uncertainty quantification for a Gaussian process, a spatial process with a computationally intensive yet tractable likelihood. However, evaluating the neural likelihood surface is faster than evaluating the exact likelihood surface by potentially orders of magnitude depending on the number of observed spatial

locations. Additionally, the approach is well-suited to determining parameter estimates using a grid-based approach which ensures that the resulting estimator is close to the global maximizer of the neural likelihood. Altogether, the neural likelihood provides comparable parameter estimation and uncertainty quantification to the exact likelihood, when one is available, along with much improved computational efficiency and guarantees for finding parameter estimators close to the global maximizer.

We have provided compelling evidence that our method produces a neural likelihood which approximates well the exact likelihood of the Brown–Resnick process, a spatial process with an intractable likelihood function. We compared neural likelihood to pairwise likelihood, a common approximation for the exact likelihood of this process. Pairwise likelihood has a tuning parameter, the distance cut-off δ , which is hard to choose optimally. Due to this tuning parameter, there is often a trade-off in terms of obtaining reasonable surfaces, parameter estimates, and approximate confidence regions. Neural likelihood, on the other hand, does not have such a tuning parameter and does not suffer from this trade-off between good parameter estimation and reasonable approximate confidence regions. In fact, when treated as an approximate likelihood function, pairwise likelihood did not produce reasonable approximate confidence regions for any distance cut-off δ we tested. Depending on the distance cut-off, neural likelihood produces comparable or better parameter estimates than pairwise likelihood in almost all cases we investigated. Additionally, the neural likelihood surface is much quicker to evaluate than the pairwise likelihood surface. Thus, we conclude that for this particular spatial process with an intractable likelihood, neural likelihood performs across the board much better than pairwise likelihood.

We conclude with a discussion of the limitations and potential extensions of our method of learning the likelihood via classification. Currently, our method learns the likelihood over a predetermined bounded parameter space which is a common assumption in contemporary simulation-based inference (e.g., Dalmaso et al., 2023) since simulating training parameters from an unbounded space is not feasible in practice. An important question for future work is to address the misspecification situation where the neural likelihood is being evaluated for a realization \mathbf{y} of the spatial process generated by a parameter $\boldsymbol{\theta}$ outside the parameter

space used to train the classifier. With active learning (Murphy, 2022, 646–647), we may be able to adaptively extend the parameter space during training in such a way that even in the misspecified case we eventually include with high probability the region that contains the true parameter θ .

Another limitation is the assumption that the spatial observations are on a fully observed regular grid of fixed size. This motivates two extensions that we plan to address in future work: First, it would be important to extend the method to partially observed grids which can probably be done by considering the unobserved locations on the grid as latent variables. Second, while often spatial data are regular, there are notable exceptions, such as Argo float data (Wong et al., 2020; Kuusela and Stein, 2018) consisting of irregularly sampled ocean temperature and salinity profiles throughout the global ocean. In the future, we would like to extend our method of learning the likelihood to such irregular spatial data, which is a nontrivial extension since the neural network and its training would need to be adapted to handle irregular inputs.

Another important topic for future work will be to investigate the robustness (Drenkow et al., 2022) of our method to input data whose distribution deviates slightly from the stochastic model used to train the network. Real-data applications may require developing techniques for addressing this distribution shift if it turns out to have a substantial impact on the performance of the network.

Finally, in this paper, we have only presented our method in terms of learning the likelihood for spatial processes. Yet, this method of learning the likelihood can extend with simple modifications beyond spatial processes to other complex statistical models. The only true requirement for the statistical model of interest is the ability to easily simulate observations from it. Altogether, this method may eventually enable efficient and accurate likelihood-based parameter estimation and uncertainty quantification for a broad range of statistical models where only approximate or computationally inefficient inference has previously been possible.

Acknowledgments

We are grateful to the members of the CMU Statistical Methods for the Physical Sciences (STAMPS) Research Group for helpful discussions and feedback throughout this work. We would also like to thank Microsoft for providing Azure computing resources for this work. J.W. and M.K. were supported in part by NSF grants DMS-2053804 and PHY-2020295 as well as NOAA grant NA21OAR4310258.

References

- Brehmer, J. and K. Cranmer (2022). Simulation-Based Inference Methods for Particle Physics. In *Artificial Intelligence for High Energy Physics*, Chapter 16, pp. 579–611. World Scientific.
- Brehmer, J., G. Louppe, J. Pavez, and K. Cranmer (2018). Mining Gold from Implicit Models to Improve Likelihood-Free Inference. *Proceedings of the National Academy of Sciences* 117, 5242 – 5249.
- Carnell, R. (2022). *lhs: Latin Hypercube Samples*. R package version 1.1.5.
- Casella, G. and R. Berger (2001, June). *Statistical Inference*. Duxbury Resource Center.
- Castruccio, S., R. Huser, and M. G. Genton (2016). High-Order Composite Likelihood Inference for Max-Stable Distributions and Processes. *Journal of Computational and Graphical Statistics* 25(4), 1212–1229.
- Chollet, F. et al. (2015). Keras. <https://keras.io>.
- Cranmer, K., J. Brehmer, and G. Louppe (2020). The Frontier of Simulation-Based Inference. *Proceedings of the National Academy of Sciences* 117(48), 30055–30062.
- Dalmaso, N., L. Masserano, D. Zhao, R. Izbicki, and A. B. Lee (2023). Likelihood-Free Frequentist Inference: Confidence Sets with Correct Conditional Coverage. arXiv:2107.03920.

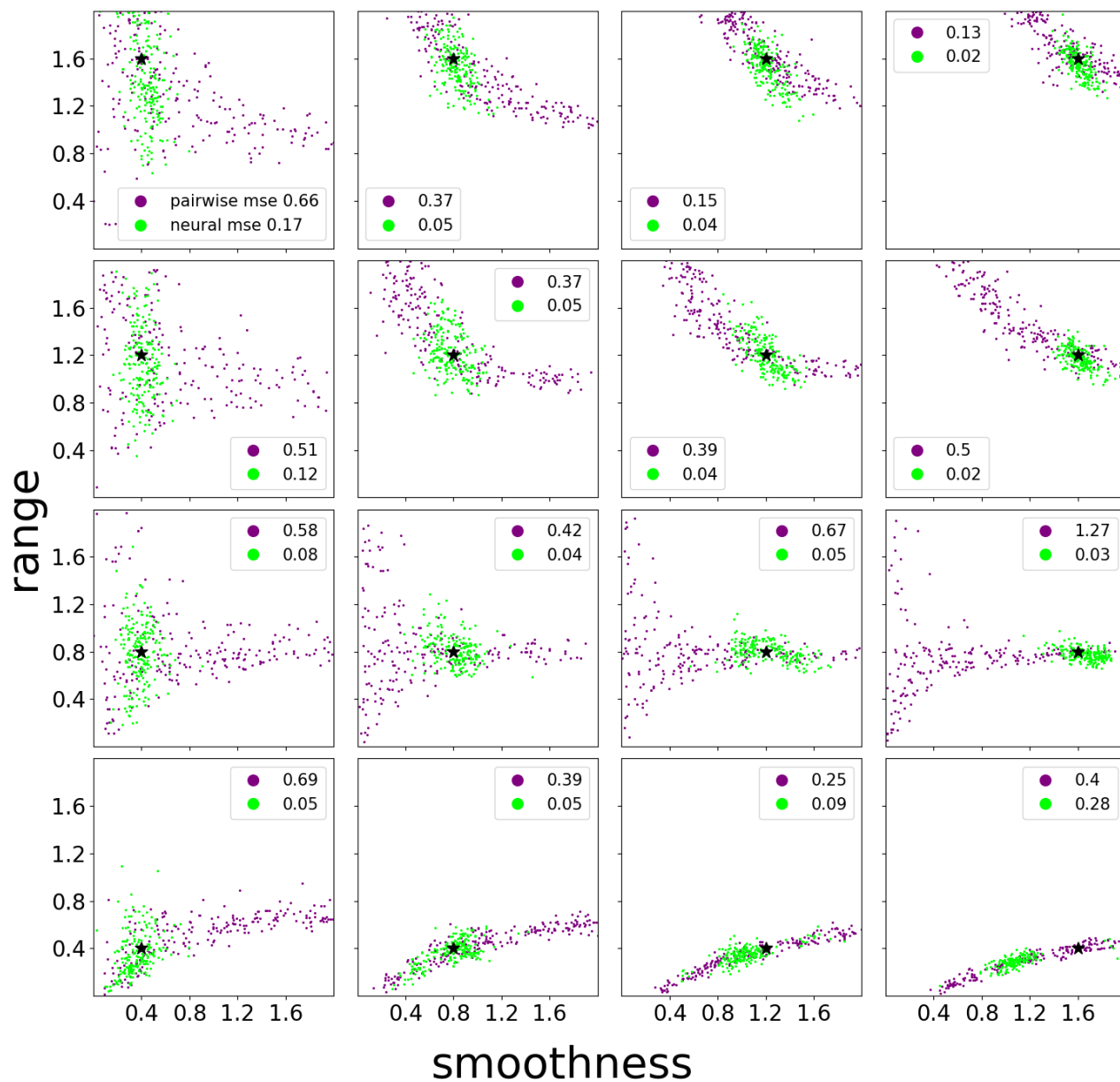
- Davison, A. C., S. A. Padoan, and M. Ribatet (2012). Statistical Modeling of Spatial Extremes. *Statistical science* 27(2), 161–186.
- Drenkow, N., N. Sani, I. Shpitser, and M. Unberath (2022). A Systematic Review of Robustness in Deep Learning for Computer Vision: Mind the Gap? arXiv:2112.00639.
- Gerber, F. and D. Nychka (2021). Fast Covariance Parameter Estimation of Spatial Gaussian Process Models using Neural Networks. *Stat* 10(1), e382.
- Goodfellow, I. J., Y. Bengio, and A. Courville (2016). *Deep Learning*. Cambridge, MA, USA: MIT Press. <http://www.deeplearningbook.org>.
- Guo, C., G. Pleiss, Y. Sun, and K. Q. Weinberger (2017). On Calibration of Modern Neural Networks. In *Proceedings of the 34th International Conference on Machine Learning - Volume 70*, ICML’17, pp. 1321–1330. JMLR.org.
- Heaton, M. J., A. Datta, A. O. Finley, R. Furrer, J. Guinness, R. Guhaniyogi, F. Gerber, R. B. Gramacy, D. M. Hammerling, M. Katzfuss, F. Lindgren, D. W. Nychka, F. Sun, and A. Zammit-Mangion (2017). A Case Study Competition Among Methods for Analyzing Large Spatial Data. *Journal of Agricultural, Biological, and Environmental Statistics* 24, 398 – 425.
- Huser, R. and A. Davison (2013). Composite Likelihood Estimation for the Brown–Resnick Process. *Biometrika* 100(2), 511–518.
- Kabluchko, Z., M. Schlather, and L. de Haan (2009). Stationary Max-Stable Fields Associated to Negative Definite Functions. *The Annals of Probability* 37(5), 2042 – 2065.
- Katzfuss, M. and J. Guinness (2021). A General Framework for Vecchia Approximations of Gaussian Processes. *Statistical Science* 36(1), 124 – 141.
- Keener, R. (2010). *Theoretical Statistics: Topics for a Core Course*. Springer Texts in Statistics. Springer New York.
- Kingma, D. and J. Ba (2015). Adam: A Method for Stochastic Optimization. *Proceedings of the 3rd International Conference on Learning Representations (ICLR 2015)*.

- Kuusela, M. and M. L. Stein (2018). Locally Stationary Spatio-Temporal Interpolation of Argo Profiling Float Data. *Proceedings of the Royal Society A* 474(2220), 20180400.
- Lecun, Y., L. Bottou, Y. Bengio, and P. Haffner (1998). Gradient-Based Learning Applied to Document Recognition. *Proceedings of the IEEE* 86(11), 2278–2324.
- Lenzi, A., J. Bessac, J. Rudi, and M. L. Stein (2023). Neural Networks for Parameter Estimation in Intractable Models. *Computational Statistics & Data Analysis* 185, 107762.
- Lindgren, F., H. Rue, and J. Lindström (2011). An Explicit Link Between Gaussian Fields and Gaussian Markov Random Fields: The Stochastic Partial Differential Equation Approach. *Journal of the Royal Statistical Society: Series B (Statistical Methodology)* 73(4), 423–498.
- Murphy, K. P. (2022). *Probabilistic Machine Learning: An Introduction*. MIT Press.
- Padoan, S. A., M. Ribatet, and S. A. Sisson (2010). Likelihood-based Inference for Max-Stable Processes. *Journal of the American Statistical Association* 105(489), 263–277.
- Platt, J. (1999). Probabilistic Outputs for Support Vector Machines and Comparisons to Regularized Likelihood Methods. *Advances in Large Margin Classifiers* 10(3), 61–74.
- Rasmussen, C. E. and C. K. I. Williams (2006). *Gaussian Processes for Machine Learning*. Adaptive computation and machine learning. MIT Press.
- Ribatet, M. (2020). *SpatialExtremes: Modelling Spatial Extremes*. R package version 2.0-9.
- Sainsbury-Dale, M., A. Zammit-Mangion, and R. Huser (2023). Neural Point Estimation for Fast Optimal Likelihood-Free Inference. arXiv:2208.12942.
- Shao, J. (2003). *Mathematical Statistics* (2nd ed.). Springer.
- Sisson, S. A., Y. Fan, and M. A. Beaumont (2018). Handbook of Approximate Bayesian Computation. Taylor and Francis.

- Sun, Y., B. Li, and M. G. Genton (2012). Geostatistics for Large Datasets. In *Advances and Challenges in Space-time Modelling of Natural Events*, Chapter 3, pp. 55–77. Berlin, Heidelberg: Springer.
- Vaart, A. W. v. d. (1998). *Asymptotic Statistics*. Cambridge Series in Statistical and Probabilistic Mathematics. Cambridge University Press.
- Wong, A., S. Wijffels, S. Riser, S. Pouliquen, S. Hosoda, D. Roemmich, J. Gilson, G. Johnson, K. Martini, D. Murphy, M. Scanderbeg, T. Udaya Bhaskar, J. Buck, F. Merceur, T. Carval, G. Maze, C. Cabanes, X. Andre, N. Poffa, and H.-M. Park (2020). Argo Data 1999–2019: Two Million Temperature-Salinity Profiles and Subsurface Velocity Observations From a Global Array of Profiling Floats. *Frontiers in Marine Science* 7(700).

6 Appendix

Neural vs Pairwise ($\delta = 1$) Parameter Estimates



Neural vs Pairwise ($\delta = 5$) Parameter Estimates

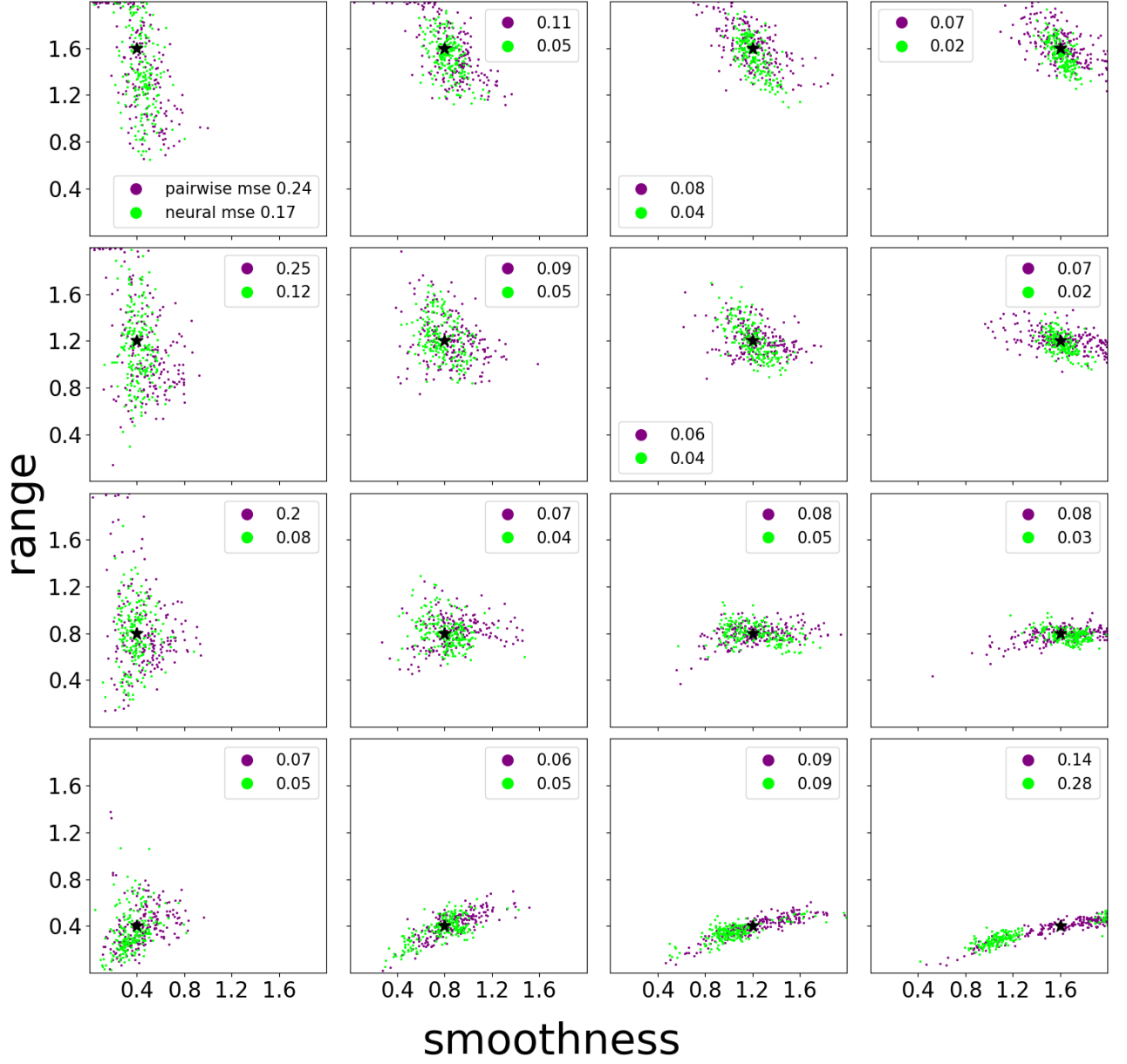
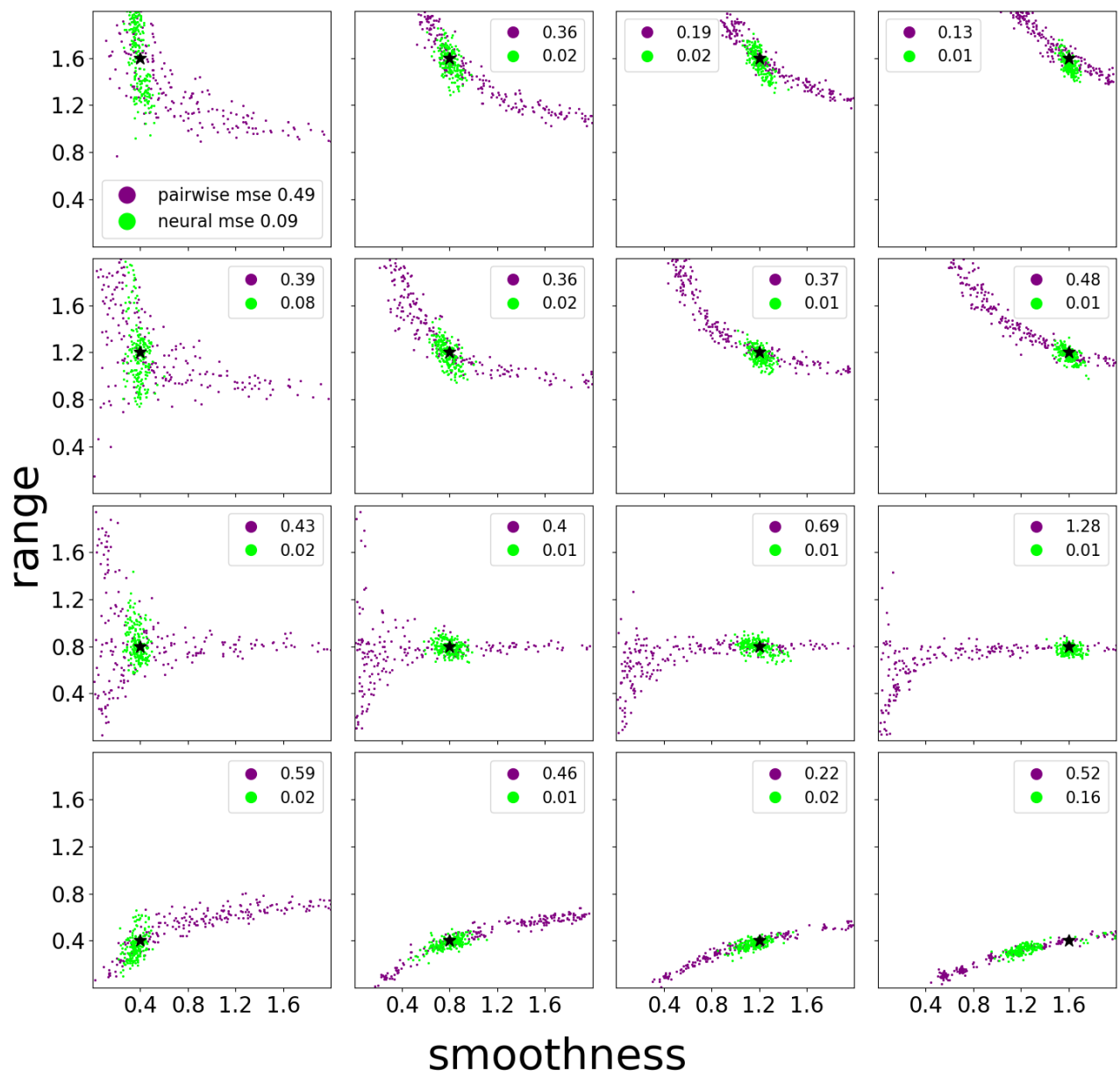


Figure 15: 4×4 plot of neural and pairwise parameter estimates for $\delta = 1, 5$. Each of the 16 plots contains the true parameter (black cross) which generated the 200 spatial field realizations and the corresponding parameter estimates for pairwise likelihood (purple) and neural likelihood (green) with mean squared error (MSE) in the legend. The true parameter increases in range from bottom to top and in smoothness from left to right.

Neural vs Pairwise ($\delta = 1$) Parameter Estimates



Neural vs Pairwise ($\delta = 5$) Parameter Estimates

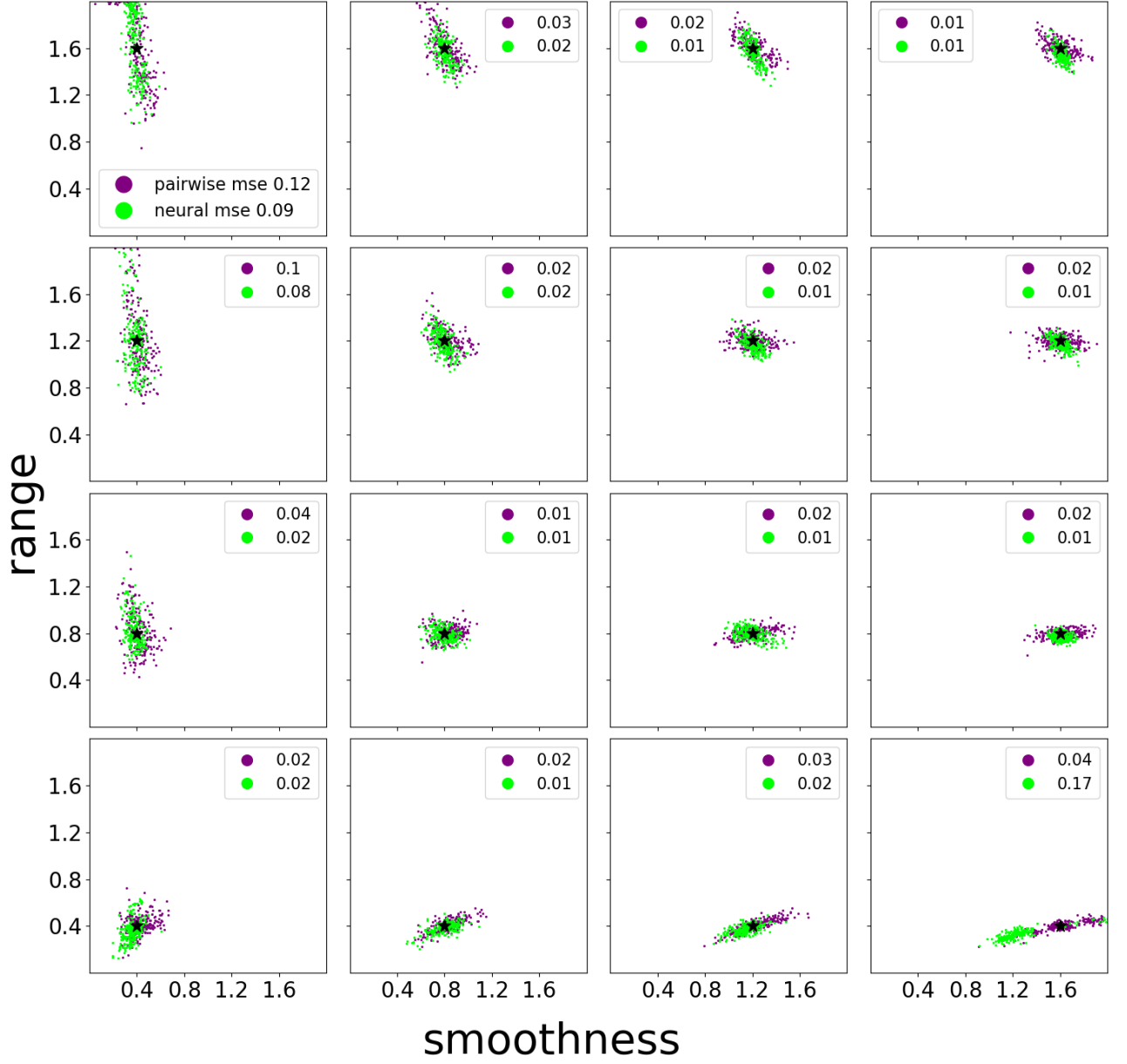


Figure 15: 4×4 plot of neural and pairwise parameter estimates for $\delta = 1, 5$ in the case of 5 i.i.d. spatial field realizations for a Brown-Resnick process. Each of the 16 plots contains the true parameter (black cross) which generated the realizations and the corresponding parameter estimates for pairwise likelihood (purple) and neural likelihood (green) with mean squared error (MSE) in the legend. The true parameter increases in range from bottom to top and in smoothness from left to right.